

# Accepted Manuscript

Carboxamides vs. methanimines: Crystal structures, binding interactions, photophysical studies, and biological evaluation of (indazole-5-yl)methanimines as monoamine oxidase B and acetylcholinesterase inhibitors

Nikolay T. Tzvetkov, Hans-Georg Stammler, Maya G. Georgieva, Daniela Russo, Immacolata Faraone, Aneliya A. Balacheva, Silvia Hristova, Atanas G. Atanasov, Luigi Milella, Liudmil Antonov, Marcus Gastreich

PII: S0223-5234(19)30568-9

DOI: <https://doi.org/10.1016/j.ejmech.2019.06.041>

Reference: EJMECH 11444

To appear in: *European Journal of Medicinal Chemistry*

Received Date: 1 June 2019

Revised Date: 13 June 2019

Accepted Date: 14 June 2019

Please cite this article as: N.T. Tzvetkov, H.-G. Stammler, M.G. Georgieva, D. Russo, I. Faraone, A.A. Balacheva, S. Hristova, A.G. Atanasov, L. Milella, L. Antonov, M. Gastreich, Carboxamides vs. methanimines: Crystal structures, binding interactions, photophysical studies, and biological evaluation of (indazole-5-yl)methanimines as monoamine oxidase B and acetylcholinesterase inhibitors, *European Journal of Medicinal Chemistry* (2019), doi: <https://doi.org/10.1016/j.ejmech.2019.06.041>.

This is a PDF file of an unedited manuscript that has been accepted for publication. As a service to our customers we are providing this early version of the manuscript. The manuscript will undergo copyediting, typesetting, and review of the resulting proof before it is published in its final form. Please note that during the production process errors may be discovered which could affect the content, and all legal disclaimers that apply to the journal pertain.



**Carboxamides vs. methanimines: Crystal structures, binding interactions, photophysical studies, and biological evaluation of (indazole-5-yl)methanimines as monoamine oxidase B and acetylcholinesterase inhibitors**

Nikolay T. Tzvetkov <sup>a,\*</sup>, Hans-Georg Stammer <sup>b</sup>, Maya G. Georgieva <sup>c</sup>, Daniela Russo <sup>d,e</sup>, Immacolata Faraone <sup>d,e</sup>, Aneliya A. Balacheva <sup>c</sup>, Silvia Hristova <sup>f</sup>, Atanas G. Atanasov <sup>g,h,i</sup>, Luigi Milella <sup>d,e</sup>, Liudmil Antonov <sup>f</sup>, Marcus Gastreich <sup>j</sup>

<sup>a</sup> NTZ Lab Ltd., Krasno selo 198, Sofia 1618, Bulgaria

<sup>b</sup> Department of Chemistry, Bielefeld University, Universitätsstr. 25, 33615 Bielefeld, Germany

<sup>c</sup> Bulgarian Academy of Sciences, Institute of Molecular Biology “Roumen Tsanev”, Department of Biochemical Pharmacology and Drug Design, Acad. G. Bonchev Str., Bl. 21, 1113 Sofia, Bulgaria

<sup>d</sup> Department of Science, Università degli Studi della Basilicata, V.le Ateneo Lucano 10, 85100 Potenza, Italy

<sup>e</sup> Spinoff BioActiPlant S.R.L. Department of Science, University of Basilicata, V.le dell'Ateneo lucano, 10, 85100 Potenza, Italy

<sup>f</sup> Bulgarian Academy of Sciences, Institute of Organic Chemistry with Centre of Phytochemistry, Acad. G. Bonchev Str., Bl. 9, Sofia 1113, Bulgaria

<sup>g</sup> Institute of Genetics and Animal Breeding of the Polish Academy of Sciences, 05-552 Jastrzebiec, Poland

<sup>h</sup> Department of Pharmacognosy, University of Vienna, Althanstrasse 14, A-1090 Vienna, Austria

<sup>i</sup> Institute of Neurobiology, Bulgarian Academy of Sciences, 23 Acad. G. Bonchev str., 1113 Sofia, Bulgaria

<sup>j</sup> BioSolveIT GmbH, An der Ziegelei 79, 53757 St. Augustin, Germany

**KEYWORDS:**

MAO-B inhibitors; Molecular modelling; (Indazole-5-yl)methanimines; Parkinson's disease; X-ray

---

\* Corresponding author.

E-mail address: ntzvetkov@ntzlab.com (N.T. Tzvetkov). Phone: +49-179-528-4358

ORCID iD: 0000-0002-8482-0481 (Dr. Nikolay T. Tzvetkov)

**Abstract**

A comprehensive study was performed for the first time to compare two structurally related substance classes, namely indazole-5-carboxamides (**11–16**) and (indazole-5-yl)methanimines (**17–22**). Both chemical entities are potent, selective and reversible MAO-B inhibitors and, therefore, may serve as promising lead structures for the development of drug candidates against Parkinson's disease (PD) and other neurological disorders. Compounds **15** ( $K_i = 170$  pM, SI = 25907) and **17** ( $K_i = 270$  pM, SI = 16340) were the most potent and selective MAO-B inhibitors in both series. To investigate the multi-target inhibitory activity, all compounds were further screened for their potency against human AChE and BuChE enzymes. Compound **15** was found to be the most potent and selective AChE inhibitor in all series ( $hAChE$   $IC_{50} = 78.3 \pm 1.7$   $\mu$ M). Moreover, compounds **11** and **17** showed no risk of drug-induced hepatotoxicity and a wider safety window, as determined in preliminary cytotoxicity screening. Molecular modeling studies into the human MAO-B enzyme-binding site supported by a HYDE analysis suggested that the imine linker similarly contributes to the total binding energy in methanimines **17–22** as the amide spacer in their carboxamide analogs **11–16**. Amplified photophysical evaluation of compounds **17** and **20**, including single X-ray analysis, photochemical experiments, and quantum-chemical calculations, provided insights into their more favourable isomeric forms and structural features, which contribute to their biologically active form and promising drug-like properties.

## 1. Introduction

Neurodegenerative diseases (NDs) are characterized by slow progressive death of neurons in the brain, leading to a loss of structure and function. Among NDs, Alzheimer's (AD) and Parkinson's disease (PD) are the two most prevalent age-related disorders of the central nervous system (CNS). As a consequence of the aging population, both NDs represent a substantial socioeconomic burden on society, currently affecting 7–8% of the population over age 65 [1–4]. Although there are common features in the cellular events that develop as a result of neurodegeneration in specific brain regions of affected patients, AD and PD display differences in pathogenesis and symptoms [3–7]. While an irreversible cognitive decline, such as severe memory, attention, and learning deficits associated with an early-onset of AD, a progressive impairment of the core motor functions is often an early indicator of PD [8–11]. AD, for example, is principally characterized by a degradation of cholinergic neurons and synapses in the neocortex and hippocampus, resulting in a decrease of acetylcholine neurotransmitter levels in these brain regions involved in higher cognitive functions [12]. The loss of dopaminergic neurons in the *substantia nigra pars compacta* (SNc) of midbrain, associated with an abnormal  $\alpha$ -synuclein aggregation as well as formation of Lewy bodies and Lewy neurites, lead to the typical symptoms of PD like resting tremor, rigidity, bradykinesia (slowness), and postural instability [9,10]. In the advanced stages, PD is accompanied by various non-motor symptoms including depression, behavioral and cognitive complications [12–14]. Thus, AD and PD are multifactorial disorders, in which complex pathophysiological processes trigger the neuronal cell impairment and death [11,15]. Therefore, disease-specific mechanisms necessitate disease-tailored therapeutic strategies.

Since an excessive loss of dopamine (DA) neurons is considered as a neuropathological hallmark of PD, the majority of the therapies introduced so far in the PD treatment have been focused on increasing the DA levels in the brain [2,16,17]. In particular, the DA replacement therapy combining the prodrug levodopa (L-DOPA) with DA agonists, DOPA-decarboxylase inhibitors (DDIs), monoamine oxidase B (MAO-B), and/or catechol-*O*-methyltransferase (COMT) inhibitors is still commonly used for PD

treatment [2,13,17–19]. However, the long-term administration of L-DOPA has been linked to major adverse effects including dyskinesia, dose failure (drug resistance), freezing during movement, but also other side effects such as DA dysregulation, hypotension, nausea, and others [17]. To date, there are only few approved drugs for AD treatment; the most of them are acetylcholinesterase (AChE) inhibitors [12,18,20]. Currently used medicines have an impact on several symptoms in different AD or PD stages by affecting mainly the brain's cholinergic or dopaminergic system, respectively, but do not change or stop the disease progression [12,18–20]. Despite enormous research efforts, including multitarget strategies rooted on the principle that a simultaneously action on two or more pharmacological targets may be beneficial for the treatment of multifactorial diseases [12,18], the medical need for new AD and PD modifying therapeutics still exists.

Monoamine oxidases (MAOs, EC 1.4.3.4) are flavoenzymes localized on the mitochondrial outer membrane that catalyze the oxidative deamination of xenobiotic and endogenous monoamines. Therefore, MAOs are important for the modulation the levels of monoamine neurotransmitters in the central and peripheral nervous system (CNS and PNS). Two isoforms, namely MAO-A and MAO-B, are present in most mammalian tissues. Both MAOs share ~73% identity of protein sequence, but display regional differences in enzyme activity, substrate specificity, and distribution in the brain and periphery [21–24]. The expression levels and activity of MAO-B, but not of MAO-A isoform, in the human brain increase ~4-fold with aging [25]. The increased activity and overexpression of MAO-B lead to an overproduction of reactive oxygen species (ROS) and, therefore, is associated with oxidative stress and loss of neuronal function [25]. In fact, increased MAO-B levels and activity is observed in the brain of PD and AD patients [26,27]. Thus, inhibition of the MAO-B isoenzyme by selective MAO-B inhibitors (IMAO-B) is an established therapeutic approach for PD treatment [28]. For example, the irreversible MAO-B inhibitors selegiline (Zelapar) and resagiline (Azilect), as well as the reversible inhibitor safinamide (Xadago) are currently in clinical use alone or as add-on therapy to L-DOPA in late-stage PD (for structures, see Fig. 1) [16,27–31].

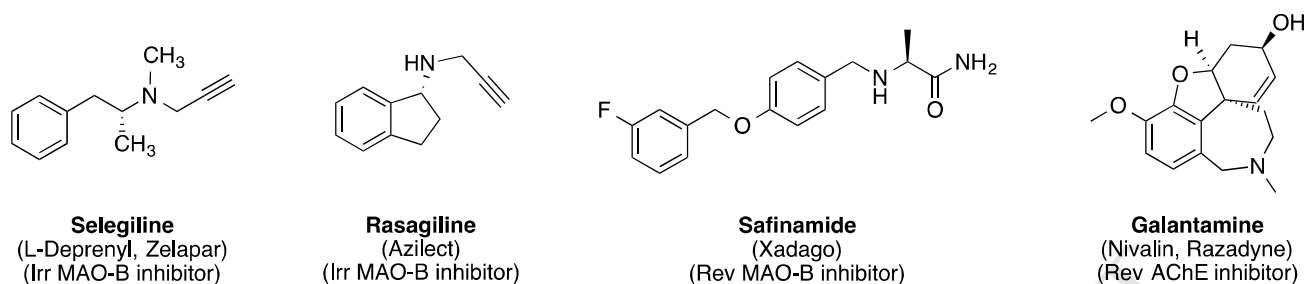


**Fig. 1.** Structures, brand names, and mechanism of action of approved drugs for PD and AD.

Acetylcholinesterase (AChE; EC 3.1.1.7) and butyrylcholinesterase (BuChE, EC 3.1.1.8) are cholinesterase (ChE) enzymes that are responsible for the hydrolysis (deacetylation) of choline-based esters, including specific neurotransmitters in both CNS and PNS [32,33]. Both ChE isoforms are ~65% identical at protein level, but differ in their substrate preference, enzyme activity, and distribution in the brain and periphery [34]. Acetylcholine (ACh) is degraded more quickly by AChE, while BuChE hydrolyses preferably butyrylcholine. In CNS, AChE is located mainly in neurons, accounting ~90% of ChE activity in the temporal cortex of the normal human brain, whereas BuChE is primary associated with glial cells and accounts ~10% of ChE activity [34]. Therefore, inhibition of AChE enzyme activity is an established therapeutic approach for AD treatment. Galantamine, for example, is a reversible AChE inhibitor of plant origin that is widely prescribed for the treatment of mild-to-moderate AD and AD-related dementia [35]. Inhibitors of BuChE may also be useful in the AD therapy due to its increased activity in advanced forms of the disease [36].

Considering their pharmacological potential and more preferable safety profile, we have been particularly focused on developing selective, reversible IMAO-B with potential multitarget activity on other CNS relevant biological targets [37–40]. Within the new chemical entities discovered by us so far, the C5-substituted indazole-carboxamide and pyrrolo-pyridine derivatives were outlined as the most favorable series for further investigation [39,40]. Consequently, we continued with exploration of compounds comprising a privileged indazole-5-carboxamide scaffold, which has provided a beneficial therapeutic potential, acting either as selective IMAO-B or dual MAO-A/B inhibitors [39] (Fig. 2).

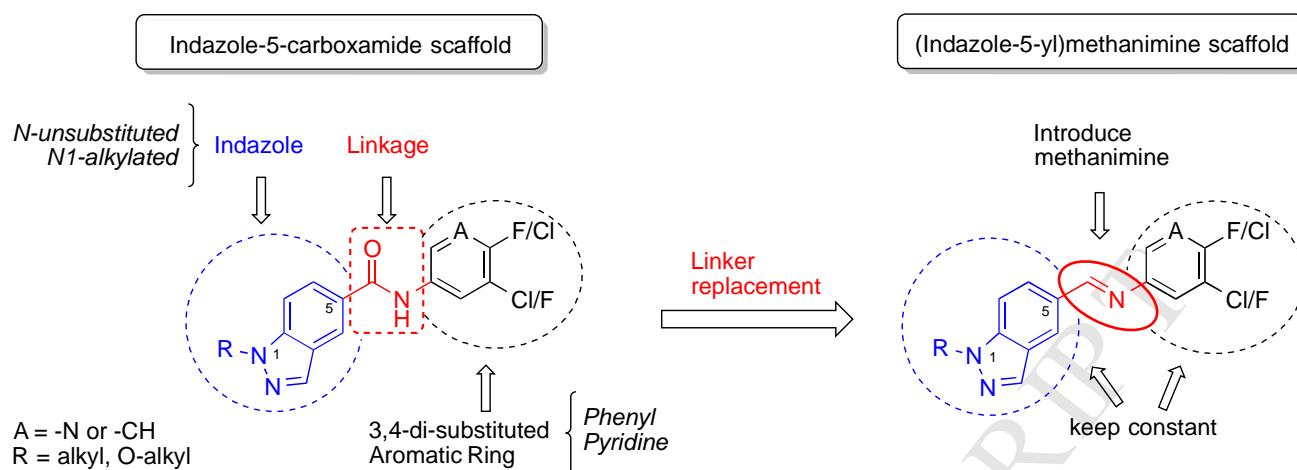


**Fig. 2.** Generic structure of previously developed selective MAO-B inhibitors **11–16** [39] (left) and intended chemical modifications towards (indazole-5-yl)methanimine scaffold (compounds **17–22**) subjected in the present work (right).

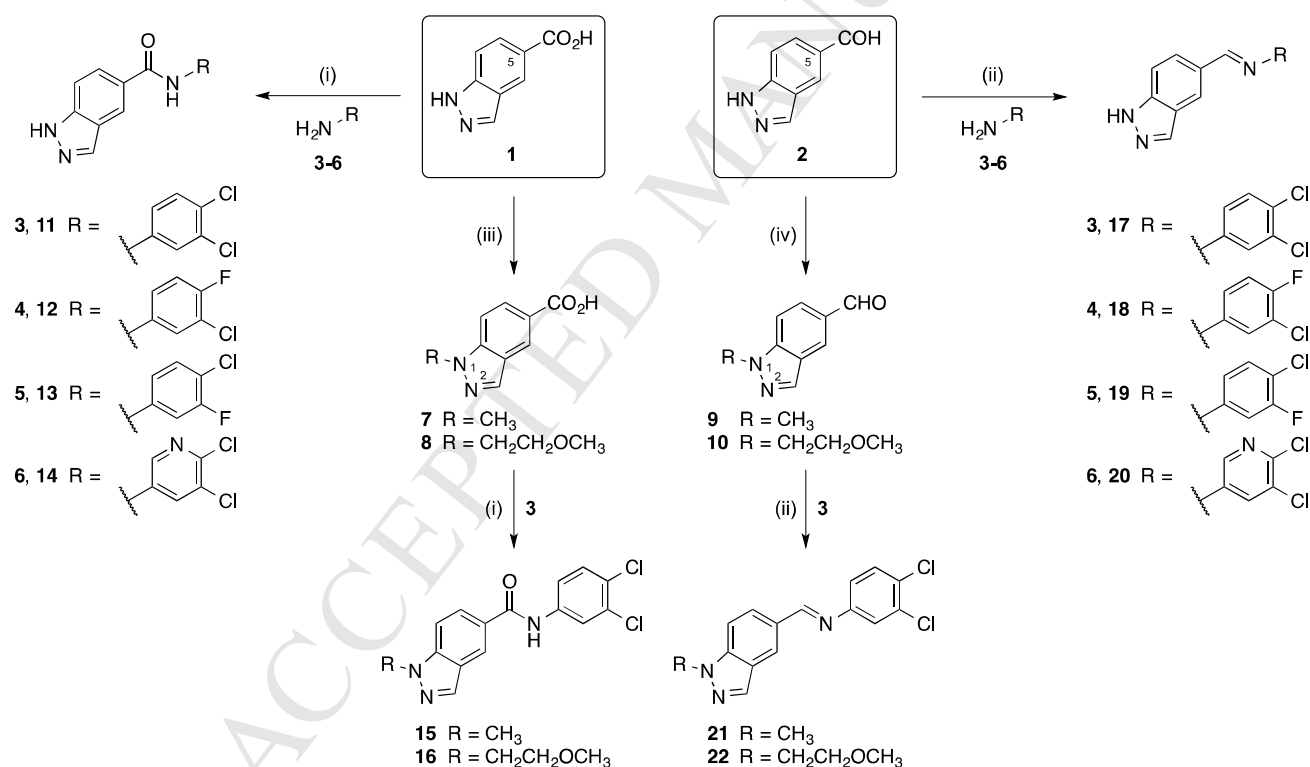
Based on previously described drug design strategy [39], facile structural modification of the key indazole-5-carboxamide scaffold (Fig. 2, left) was performed to replace the carboxamide spacer by an imine linker, obtaining a series of (indazole-5-yl)methanimine derivatives (Fig. 2, right).

In the present work, we performed a comprehensive study to compare two structurally related substance classes, namely indazole-5-carboxamides and (indazole-5-yl)methanimines. Both series of compounds were tested at human MAO-A and B, and further screened for their inhibitory activity against human AChE and BuChE enzymes. Furthermore, we evaluated kinetics, mechanism of MAO-B inhibition, drug-like and physicochemical properties, as well as the cytotoxic effects of representative IMAO-B. To understand the most important inhibitor–enzyme interactions within the binding pocket of different pharmacological targets, docking experiments were conducted using the single X-ray structures of selected compounds under study. Photophysical experiments under different conditions supported by quantum-chemical calculations were performed to investigate the more stable isomeric forms (e.g., *E/Z*-isomers and tautomers), as well as the photochemical stability of selected (indazole-5-yl)methanimine derivatives. Finally, Pan assay interference properties (PAINS) of the studied compounds were investigated and discussed.

## 2. Results and discussion

### 2.1. Chemistry

Synthesis and chemical structures of compounds under study are shown in Scheme 1. The preparation of indazole-5-carboxamide derivatives **11–16** was performed following optimized reaction procedures to obtain the compounds in higher yields (>81% yield in average) [39]. Accordingly, compounds **11–14** can be prepared via amide coupling reaction of 1*H*-indazole-5-carboxylic acid (**1**) with the appropriate 3,4-disubstituted anilines **3–6** using EDC hydrochloride as a coupling reagent (Scheme 1, left). The N1-alkylated indazole-5-carboxamide derivatives **15** and **16** can be synthesized following a four-step regioselective approach [39].



**Scheme 1.** Synthetic routes to indazole-5-carboxamides **11–16** and (indazole-5-yl)methanimines **17–22**. Reagents and conditions: (i) EDC–HCl, methanol, r.t., 3–16 h; (ii) conc. acetic acid (10 mol-%), ethanol, reflux, 1–24 h; (iii) 1) methanol, c. H<sub>2</sub>SO<sub>4</sub> (10 mol-%), 60–70 °C, 1–3 h, 2) methyl methanesulfonate (MMS, for **15**) or 1-bromo-2-methoxyethane (for **16**), K<sub>2</sub>CO<sub>3</sub>, DMF, reflux, 9–16 h, 3) 2M NaOH, THF–H<sub>2</sub>O (1:1), 30–35 °C, 1–3 h; (iv) MMS (for **9**) or 1-bromo-2-methoxyethane (for **10**), K<sub>2</sub>CO<sub>3</sub>, DMF, reflux, 68–72 h.

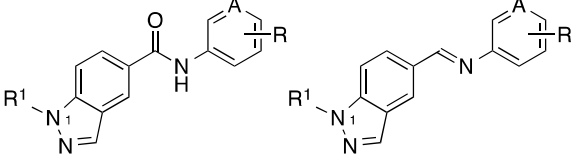
For the preparation of methanimines **17–20**, 1*H*-indazole-5-carbaldehyde (**2**) was reacted with the respective anilines **3–6** in the presence of a catalytic amount of acetic acid in ethanol under reflux (Scheme 1, right). The N1-alkylated aldehydes **9** and **10** can be prepared via one-step synthetic procedure (for **10**, see Supporting Information). Subsequently, aldehydes **9** and **10** were condensed with 3,4-dichloroaniline (**3**) to obtain the N1-alkylated methanimines **21** and **22**, respectively. To investigate the chemical stability of methanimines **17–22** (i.e., Schiff bases), extensive stability studies for selected compounds were performed (see Section 2.5.1 and Supporting Information). All final products were purified by column chromatography following by recrystallization and their structures confirmed by NMR spectroscopy and mass spectrometry. The described procedures allow the introduction of further structural modifications, to access small compound libraries for rapid evaluation of structure-activity relationships (SARs). In addition, we obtained the single X-ray structures of **17** and **20**, confirming not only the preferable formation of the 1*H*-indazole tautomeric form, but also the *trans*-isomerism of (indazole-5-yl)methanimine derivatives **17–22** (see Section 2.5.2 and Supporting Information).

## 2.2. Biological evaluation

Biological evaluation of all compounds toward human (*h*) MAOs and human ChEs (*h*AChE and *h*BuChE) was performed according to established protocols [39–42].

### 2.2.1. Monoamine oxidase studies

The enzyme inhibition of the studied compounds against MAOs was performed using a fluorescence-based assay with *p*-tyramine as a substrate and the commercial kit Amplex Red [43,44]. Determined *in vitro* MAOs inhibitory activities (IC<sub>50</sub> values) and selectivity (expressed as selectivity index, SI) toward *h*MAO-B for all compounds and reference inhibitors are shown in Table 1. Determination of the kinetic parameters ( $K_m$  and  $V_{max}$ ) of the *h*MAO-B enzyme was performed at different concentrations of *p*-tyramine and the  $K_i$  values of the tested compounds were obtained using the Cheng-Prusoff equation (see also Experimental Section) [45].

**Table 1** Monoamine oxidase activity and selectivity of the tested compounds.


A = CH, 11-13, 15, 16  
A = N, 14

A = CH, 17-19, 21, 22  
A = N, 20

Compd.	R	R <sup>1</sup>	IC <sub>50</sub> ± SEM (nM) <sup>a</sup>			K <sub>i</sub> ± SEM (nM) <sup>a,c</sup>
			hMAO-A	hMAO-B	SI <sup>b</sup>	
<b>11</b> (NTZ-1006)	3,4-Cl	H	≥10000	0.586 ± 0.087 <sup>d</sup>	17065	0.26 ± 0.04
<b>12</b>	3-Cl, 4-F	H	>10000	0.679 ± 0.044 <sup>e</sup>	14727	0.30 ± 0.02
<b>13</b>	3-F, 4-Cl	H	>10000	0.668 ± 0.053 <sup>d</sup>	14970	0.29 ± 0.02
<b>14</b>	3,4-Cl	H	>10000	5.42 ± 0.20 <sup>d</sup>	>1845	2.39 ± 0.18
<b>15</b> (NTZ-1091)	3,4-Cl	Me	>10000	0.386 ± 0.052 <sup>e</sup>	25907	0.17 ± 0.02
<b>16</b>	3,4-Cl	EtOMe	2870 ± 218 <sup>e</sup>	1.08 ± 0.08 <sup>e</sup>	>2657	0.48 ± 0.04
<b>17</b>	3,4-Cl	H	>10000	0.612 ± 0.065 <sup>d</sup>	16340	0.27 ± 0.03
<b>18</b>	3-Cl, 4-F	H	>10000	2.10 ± 0.30	4762	0.93 ± 0.13
<b>19</b>	3-F, 4-Cl	H	>10000	1.91 ± 0.27	5236	0.84 ± 0.12
<b>20</b>	3,4-Cl	H	>10000	1.28 ± 0.02	>7812	0.57 ± 0.02
<b>21</b>	3,4-Cl	Me	>10000	1.03 ± 0.09 <sup>d</sup>	9709	0.46 ± 0.08
<b>22</b>	3,4-Cl	EtOMe	4072 ± 272	1.29 ± 0.08	3157	0.57 ± 0.07
<b>Selegiline</b>	–	–	1424 ± 69.1 <sup>f</sup>	5.50 ± 0.26 <sup>f</sup>	259	na
<b>Rasagiline</b>	–	–	680 ± 129 <sup>f</sup>	13.0 ± 0.90 <sup>f</sup>	>52	na
<b>Safinamide</b>	–	–	>25900 <sup>g</sup>	5.18 ± 0.04 <sup>g</sup>	5000 <sup>g</sup>	2.29 ± 0.02 <sup>g</sup>

<sup>a</sup> n = 3, unless otherwise noted. <sup>b</sup> Selectivity index: SI = IC<sub>50</sub>(hMAO-A)/IC<sub>50</sub>(hMAO-B). <sup>c</sup> The experimentally measured IC<sub>50</sub> hMAO-B values were converted to the respective inhibition constants (K<sub>i</sub>) using Cheng-Prusoff equation: K<sub>i</sub> = IC<sub>50</sub>/(1 + [S]/K<sub>m</sub>) with [S] = 150 μM and K<sub>m</sub> = 118.8 μM. <sup>d</sup> Data are from ref. [37]. <sup>e</sup> Data are from ref. [39]. <sup>f</sup> Data are from ref. [46]. <sup>g</sup> Data are from ref. [40]. h = human, na = non-applicable.

### 2.2.1.1. Evaluation of inhibitory activities at human MAOs

In the present study we aimed to perform a comparative study within the series of indazole-5-carboxamide (designated subclass I, compounds **11–16**) and (indazole-5-yl)methanimine (subclass II, **17–22**) derivatives with respect to: (i) inhibition of both MAO-A and MAO-B isoforms, (ii) inhibitory activities against both *hAChE* and *hBuChE* enzymes, (iii) toxicological effects, and (iv) their photophysical and quantum-chemical investigation of isomerism and photochemical stability.

For evaluation of SARs of the compounds in Table 1, rasagiline and safinamide were used as reference for irreversible and reversible MAO-B inhibitors, respectively. The selective irreversible inhibitors clorgyline and selegiline were also used as positive controls in the MAO-A and MAO-B assays, respectively. In general, all tested compounds are selective and potent inhibitors of human MAO-B with  $IC_{50}$  values ranging from low nanomolar to even picomolar potency (*hMAO-B*). With the exception of the N1-methoxyethyl-substituted subclass I compound **16** and its subclass II analog **22**, neither of the remaining carboxamide derivatives (compounds **11–15**) or their methanimine analogs (**17–21**) exhibited noticeable inhibition of MAO-A at the highest tested concentration of 10  $\mu$ M.

In this study, compounds **11–16** (subclass I) were included to better compare the effects of a spacer modification on inhibition potency and selectivity at both MAO isoforms with those of **17–22** (subclass II). Therefore, in order to investigate the role of such small modification within both series of compounds (e.g., carboxamides vs. methanimines), we retained the 3,4-dihalo-substitution at the phenyl ring and the C5-substituted indazole moiety unit during further exploration. Replacement of the carboxamide spacer in subclass I compounds **11–16** by an amine function resulted in potent and selective IMAO-B (subclass II compounds **17–22**). Nevertheless, methanimines **17–22** displayed almost equally high affinity toward MAO-B compared to their carboxamide analogs **11–16**.

The 3,4-dichlorophenyl indazole-5-carboxamide **11** was the most potent and selective IMAO-B within the indazole *N*-unsubstituted subclass I compounds ( $IC_{50} = 0.586$  nM; SI = 17065), while its methanimine analog **17** represents the most active and selective IMAO-B within the subclass II series

( $IC_{50} = 0.612$  nM;  $SI = 16340$ ). Compounds **11** and **17** exhibited almost equally improved *h*MAO-B inhibitory activity when compared to the standard IMAO-B, being ~9-fold more potent than selegiline and safinamide. Further structural modifications of **11** and **17** were performed by replacement of the 4-Cl or the 3-Cl atoms at the phenyl ring with one fluorine atom (compounds of subclass I **12**, **13** and subclass II **18**, **19**). The respective 3-chloro-4-fluoro- or 4-chloro-3-fluoro-substituted carboxamides (compounds **12** and **13**) were almost equipotent and selective inhibitors of *h*MAO-B (**12**,  $IC_{50} = 0.68$  nM,  $SI = 14727$ ; **13**,  $IC_{50} = 0.67$  nM,  $SI = 14,970$ ), comparable to the inhibitory activity of **11**. In contrast, the presence of 3-chloro-4-fluoro (compound **18**,  $IC_{50} = 2.19$  nM,  $SI = 4672$ ) and 4-chloro-3-fluoro substituents (**19**,  $IC_{50} = 1.91$  nM,  $SI = 5236$ ) at the phenyl ring of subclass II compounds led to a decrease in inhibitory activity and selectivity against *h*MAO-B, when compared to the potency and selectivity of the parent methanimine **17** and the respective carboxamide analogs **12** and **13** (subclass I). It is worth mentioning that the respective 3-fluoro-4-chlorophenyl-substituted derivatives in both series (e.g., carboxamide **13** and methanimine **19**) were slightly more active at *h*MAO-B enzyme than their 4-chloro-3-fluorophenyl-substituted analogs **12** and **18**, respectively.

Next, the phenyl ring of **11** and **17** was replaced by a bioisosteric 5,6-dichloropyridine residue in order to enhance water solubility of both lipophilic series of IMAO-B. The resulting carboxamide and methanimine derivatives **14** (subclass I) and **20** (subclass II) are less active than the respective 3,4-dichloro-phenyl analogs **11** and **17**, but they are still potent IMAO-B (**14**,  $IC_{50} = 5.42$  nM; **20**,  $IC_{50} = 1.28$  nM). Interestingly, methanimine **19** is the only compound within subclass II IMAO-B exhibiting higher inhibitory activity against *h*MAO-B than its carboxamide analog (i.e., subclass I compound **14**). In comparison to **14**, compound **20** is ~4.2- and ~4.9-fold more potent against human and rat MAO-B, respectively. Compared to selegiline and safinamide, methanimine **20** displays a ~4.3- and ~4.6-fold increase in inhibitory potency towards *h*MAO-B, respectively, while carboxamide **14** is similarly potent as both standard IMAO-B.

Introduction of a methyl group at the indazole N1 position in **11** and **17** resulted in compounds **15** and **21**. The N1-methylated carboxamide **15** was found to be the best IMAO-B of all compounds under study (human  $IC_{50} = 0.386$  nM, rat  $IC_{50} = 1.32$  nM, SI = 25907), being almost 2- and >13-fold more potent than its precursor **11** and safinamide, respectively. The respective N1-methylated methanimine (compound **21**) provided to be weaker IMAO-B than the precursor **17** and the subclass I analog **15**. However, compound **21** ( $IC_{50} = 1.03$  nM) was 5-fold more potent against *h*MAO-B than safinamide ( $IC_{50} = 5.18$  nM). The elongation of the N1-alkyl substitution by introducing of a larger methoxyethyl group in compounds of subclass I (carboxamide **16**) and subclass II (methanimine **22**) generally provided potent and selective IMAO-B. Both compounds are similarly potent against MAO-B (**16**,  $IC_{50} = 1.08$  nM; **22**,  $IC_{50} = 1.29$  nM), displaying a 4- and 5-fold increase in inhibitory activity toward *h*MAO-B than safinamide, respectively. As mentioned above, the N1-methoxyethyl-substituted derivatives **16** and **22** are the only representatives in these series showing inhibitory activity against *h*MAO-A enzyme (**16**,  $IC_{50} = 2870$  nM; **22**,  $IC_{50} = 4072$  nM).

In addition, the respective  $IC_{50}$  values for all compounds under study were compared with the corresponding inhibitory constants  $K_i$ , which were obtained and calculated from the *h*MAO-B enzyme kinetic experiments (Table 1). A good agreement between the  $IC_{50}$  and  $K_i$  values (low nM range) for all compounds could be observed. The estimated  $K_i$  values reveal of a competitive mode of inhibition (for competitive inhibitors:  $K_i \leq IC_{50}/2$ , if  $S \sim K_m$ ) [45,47].

#### 2.2.1.2. Evaluation of mechanism of monoamine oxidase B inhibition

Due to the preferable safety profile compared to irreversible MAO inhibition, we were particularly interested in development of reversible IMAO-B [39]. Therefore, time-dependent studies with the most potent N1-methyl-substituted compound **15** (indazole-5-carboxamide, subclass I) and its (indazole-5-yl)methanimine analog **21** (subclass II) were performed to investigate whether both representative compounds are reversible or irreversible MAO-B inhibitors (Fig. 3). The mode of interaction with the active site of *h*MAO-B by **15** and **21** and standard MAO-B inhibitors selegiline (irreversible, Irr) and

safranamide (reversible, Rev) was measured after the first 15 min in the presence of low concentration of *p*-tyramine (10  $\mu$ M) and over 300 min after increasing the substrate concentration. A continuous enhancement on enzymatic residual activity could be detected for compounds **15**, **21** and safranamide after increasing the concentration of *p*-tyramine at 1.0 mM, while no significant elevation in fluorescence was measured across the time for selegiline. The experiments are in agreement with the observed correlation between the  $IC_{50}$  and  $K_i$  values of **15** and **21** at *h*MAO-B ( $IC_{50} = 0.39$  nM and  $K_i = 0.17$  nM for **15**;  $IC_{50} = 1.03$  nM and  $K_i = 0.46$  nM for **21**) revealing a reversible MAO-B inhibition.

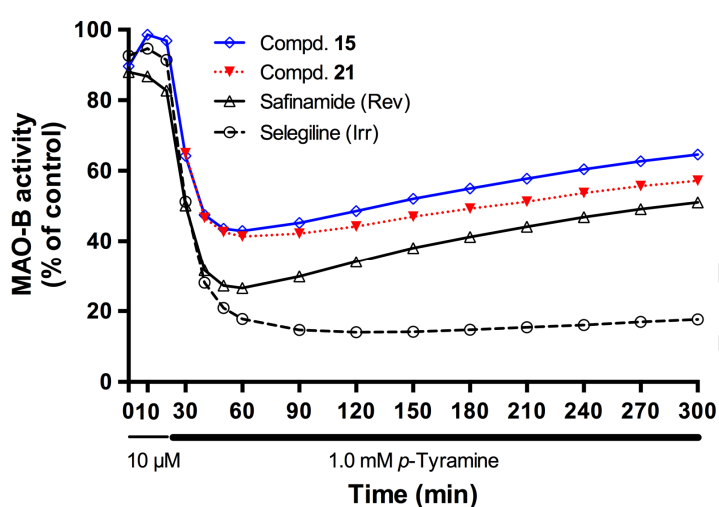


**Fig. 3.** Time-dependent inhibition (reactivation) of *h*MAO-B enzyme by the standard irreversible IMAO-B selegiline (Irr, 30 nM), reversible IMAO-B (Rev, 50 nM), and compounds **15** and **21** (both at 1.0 nM). The substrate concentration was increased from 10  $\mu$ M to 1.0 mM during a period of 300 min. The remaining *h*MAO-B enzyme activity is expressed as % of control sample used in the experiment. The values are the mean  $\pm$  SD ( $n = 4$ ).

In order to investigate the type of *h*MAO-B inhibition of **15** and **21**, Michaelis-Menten kinetics experiments were performed (Fig. 4). Accordingly, the initial rates of the deamination reaction of *p*-tyramine (at six different concentrations) catalyzed by *h*MAO-B in the absence (no inhibitor) and in the presence of different concentrations of **15** and **21** (with the respective inhibitor at 0.5, 1.0 and 5.0 nM) were measured. From the obtained Lineweaver-Burk plots, representing the reciprocal *h*MAO-B enzyme activity vs. the reciprocal *p*-tyramine concentration, we observed that both compounds acted as competitive IMAO-B. The Lineweaver-Burk plots are linear and intersected at the y-axis together with

the plot for the uninhibited *h*MAO-B (without inhibitor), which is in agreement with our previously findings [48]. The *h*MAO-B enzyme binding affinities (inhibition constants  $K_i$ ) obtained from the respective Dixon plots ( $K_i = 0.22$  nM for **15**;  $K_i = 0.63$  nM for **21**) correlate very well with the determined  $IC_{50}$  and the calculated  $K_i$  values for **15** ( $IC_{50} = 0.39$  nM,  $K_i = 0.17$  nM) and **21** ( $IC_{50} = 1.03$  nM,  $K_i = 0.46$  nM), respectively (cf. Table 1). The results obtained from the reactivation and the kinetic experiments of **15** and **21** indicate that indazole-5-carboxamides (compounds **11–16**) and (indazole-5-yl)methanimine derivatives (compounds **17–22**) are reversible and competitive MAO-B inhibitors.

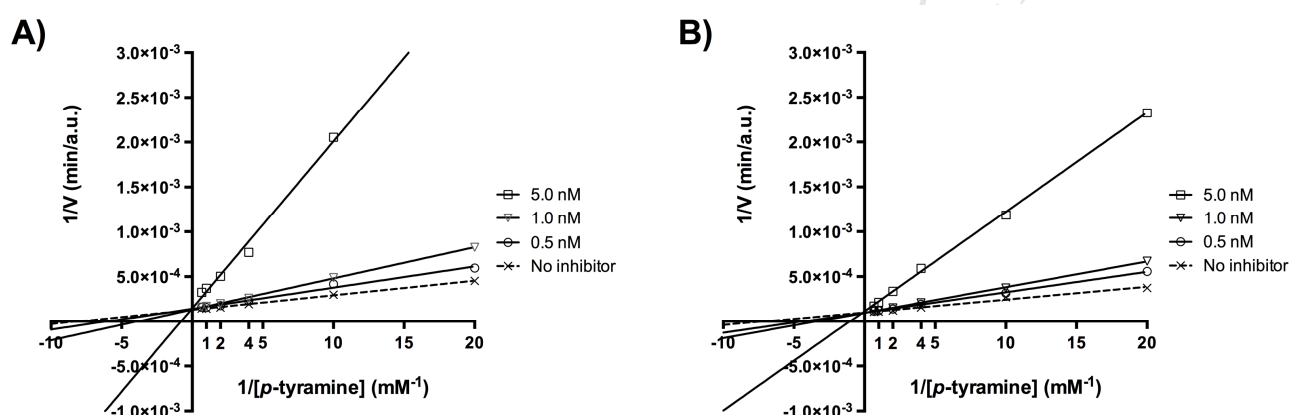


**Fig. 4.** Kinetic studies on the mechanism of *h*MAO-B inhibition of compounds **15** (A) and **21** (B). The mode of *h*MAO-B inhibition was evaluated from the respective double reciprocal Lineweaver-Burk plots of 1/rate ( $1/V$ ) vs.  $1/p$ -tyramine substrate concentration in the presence of different concentrations of the inhibitors (0.5, 1.0 and 5.0 nM).

### 2.2.2. Evaluation of cholinesterase inhibitory activity

In order to investigate the activity on other CNS relevant biological targets, all compounds also were screened for inhibition of *h*AChE and *h*BuChE in a concentration range of 10 to 100  $\mu$ M (Fig. S3 and S4). With exception of the N1-methylated indazole-5-carboxamide **15** at *h*AChE ( $IC_{50} = 78.3 \pm 1.7$   $\mu$ M), none of the remaining compounds displayed inhibitory activity below 100  $\mu$ M range toward both ChE isoforms (Table 2). Similarly to **15**, its N1-methylated (indazole-5-yl)methanimine analog (compound **21**) was found to be the most active derivative in the series of subclass II compounds ( $IC_{50} = 118.8 \pm 1.1$   $\mu$ M). However, an accurate SAR evaluation of the cholinesterase assays data suggest that

indazole N1 position could be essential for achievement of multi-target active compounds in both series. Thus, further experimental studies are required in order to find the optimal substitution pattern of the indazole moiety. The experimental data are in agreement with the results obtained from *in silico* evaluation of binding affinities toward both *hChEs* (see Fig. S7).

**Table 2** Cholinesterase activity of the tested compounds.

Compd.	Inhibition % at 100 $\mu\text{M}$ (or $\text{IC}_{50}$ , $\mu\text{M}$ ) <sup>a</sup>	
	<i>hAChE</i>	<i>hBuChE</i>
<b>11</b>	21.6 $\pm$ 0.6 (>100, UTC <sup>b</sup> )	11.3 $\pm$ 0.5 (>100, UTC <sup>b</sup> )
<b>12</b>	26.4 $\pm$ 2.1 (>100, UTC <sup>b</sup> )	7.21 $\pm$ 1.39 (>100, UTC <sup>b</sup> )
<b>13</b>	14.2 $\pm$ 1.2 (>100, UTC <sup>b</sup> )	2.23 $\pm$ 0.28 (>100, UTC <sup>b</sup> )
<b>14</b>	6.87 $\pm$ 1.13 (>100, UTC <sup>b</sup> )	9.23 $\pm$ 0.21 (>100, UTC <sup>b</sup> )
<b>15</b>	17.9 $\pm$ 1.7 (78.3 $\pm$ 1.1) <sup>c</sup>	11.1 $\pm$ 1.4 (>100, UTC <sup>b</sup> )
<b>16</b>	8.66 $\pm$ 1.98 (>100, UTC <sup>b</sup> )	9.58 $\pm$ 1.01 (>100, UTC <sup>b</sup> )
<b>17</b>	11.1 $\pm$ 1.6 (>100, UTC <sup>b</sup> )	9.01 $\pm$ 0.57 (>100, UTC <sup>b</sup> )
<b>18</b>	24.6 $\pm$ 2.7 (>100, UTC <sup>b</sup> )	4.56 $\pm$ 0.52 (>100, UTC <sup>b</sup> )
<b>19</b>	9.69 $\pm$ 0.64 (>100, UTC <sup>b</sup> )	6.97 $\pm$ 0.78 (>100, UTC <sup>b</sup> )
<b>20</b>	6.92 $\pm$ 0.76 (>100, UTC <sup>b</sup> )	9.64 $\pm$ 1.06 (>100, UTC <sup>b</sup> )
<b>21</b>	11.9 $\pm$ 0.7 (>100, UTC <sup>b</sup> )	8.57 $\pm$ 2.14 (>100, UTC <sup>b</sup> )
<b>22</b>	6.91 $\pm$ 0.74 (>100, UTC <sup>b</sup> )	2.27 $\pm$ 0.40 (>100, UTC <sup>b</sup> )
<b>Galantamine</b>	71.2 $\pm$ 2.3 (3.03 $\pm$ 0.39) <sup>c</sup> (0.80 $\pm$ 0.06) <sup>d</sup>	38.3 $\pm$ 4.1 (16.5 $\pm$ 1.2) <sup>c</sup> (7.30 $\pm$ 0.83) <sup>d</sup>

<sup>a</sup> Data are means  $\pm$  SD of three independent experiments. <sup>b</sup> Compounds did not reach 50% inhibition at 100  $\mu\text{M}$ , i.e., calculation of an  $\text{IC}_{50}$  value within the curvature was not possible (>100  $\mu\text{M}$ , UTC = unable to calculate). <sup>c</sup>  $\text{IC}_{50}$  values were determined by extrapolating the curvature of log (inhibitor) vs. normalized response with a variable slope in GraphPad Prism 6.0 (GraphPad Software) resulting in the respective  $\mu\text{M}$   $\text{IC}_{50}$  values. <sup>d</sup> Data are from ref. [49].

### 2.3. Evaluation of cytotoxicity

The preliminary cytotoxicity of the parent *N*-unsubstituted indazole-carboxamide **11** (subclass I) and methanimine **17** (subclass II) compounds were evaluated by the determination of the cellular viability in human hepatocarcinoma cells (HepG2 cell line). Cellular viability was estimated after 72 hours incubation period in a concentration range of 0.1 to 50  $\mu$ M using the methylthiazolyldiphenyl-tetrazolium bromide (MTT) reduction assay (Fig. 5). In the MTT assay, the yellow tetrazolium salt (MTT) is reduced in metabolically active cells to an insoluble purple formazan, which is then spectrophotometrically quantified to provide a direct measure of normal mitochondrial function or dysfunction (in case of cytotoxic effects of tested compounds) [50]. The HepG2 cell line is often used in the preclinical safety assessment to predict a drug's potential to cause hepatotoxicity [51].

In general, the hepatotoxicity profile of compounds **11** (Fig. 6A) and **17** (Fig 6B) followed the same trend in hepatocarcinoma cells, when compared to the control groups at all tested concentrations. For both compounds, no pronounced decrease on cellular viability was detected at the highest tested concentration of 50  $\mu$ M (**11**, HepG2:  $66.3 \pm 6.82\%$ ; **17**, HepG2:  $80.6 \pm 8.13\%$ ).

Since no major effects were observed in the MTT reduction assay after 72 h incubation period, it could be concluded that the respective indazole-5-carboxamide (subclass I **11**) and (indazole-5-yl)methanimine (subclass II **17**) derivatives did not show a pronounced mitochondrial dysfunction on HepG2 cells even at the highest tested concentrations of 25 and 50  $\mu$ M, suggesting no risk of drug-induced hepatotoxicity and a wide safety window. However, for further preclinical studies, additional examination of toxicology and genotoxicity of selected drug candidates need to be performed.

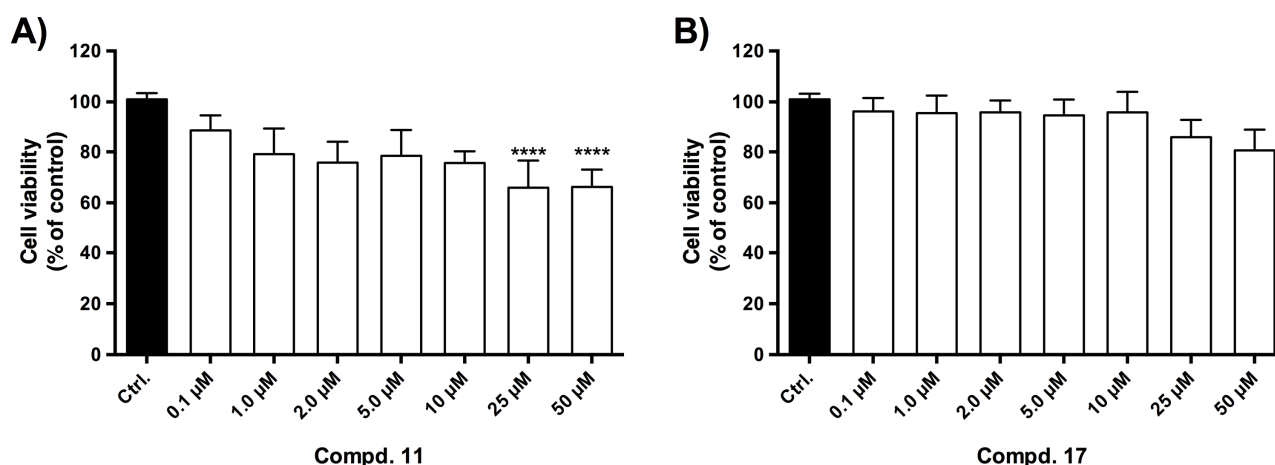


**Fig. 5.** Cytotoxicity profile of compounds **11** (A) and **17** (B) measured on human hepatocarcinoma HepG2 cells after a 72 h exposure to different concentrations of compounds (0.1 to 50  $\mu$ M). Untreated cells were used as positive control and the results are expressed as the mean % of untreated controls  $\pm$  SD ( $n = 4$ ). \*\*\*\*  $p < 0.0001$  vs. control.

## 2.4. Molecular modeling studies

### 2.4.1. Single X-ray structures of **17** and **20**

In order to investigate the binding mode and interactions of the indazole-5-carboxamide derivatives **11–16** and their (indazole-5-yl)methanimine analogs **17–22** within the *h*MAO-B enzyme active site, the single crystal X-ray structures of the most active subclass II compound **17** and its pyridine-substituted analog **20** were obtained and then used as crystallographic templates for docking studies (see Section 2.3.2 and Supporting Information).

The respective single X-ray structures of compounds **17** and **20** with atom numbering are shown in Fig. 6. Similarly to the crystal structures of subclass I compounds **11** and **15** (cf. Fig. S5) [39], the X-ray structural analyses of **17** and **20** confirm their almost planar conformation. Relevant experimental details for the X-ray analysis of both compounds are given in Table S3 and S4 (see Supporting Information).

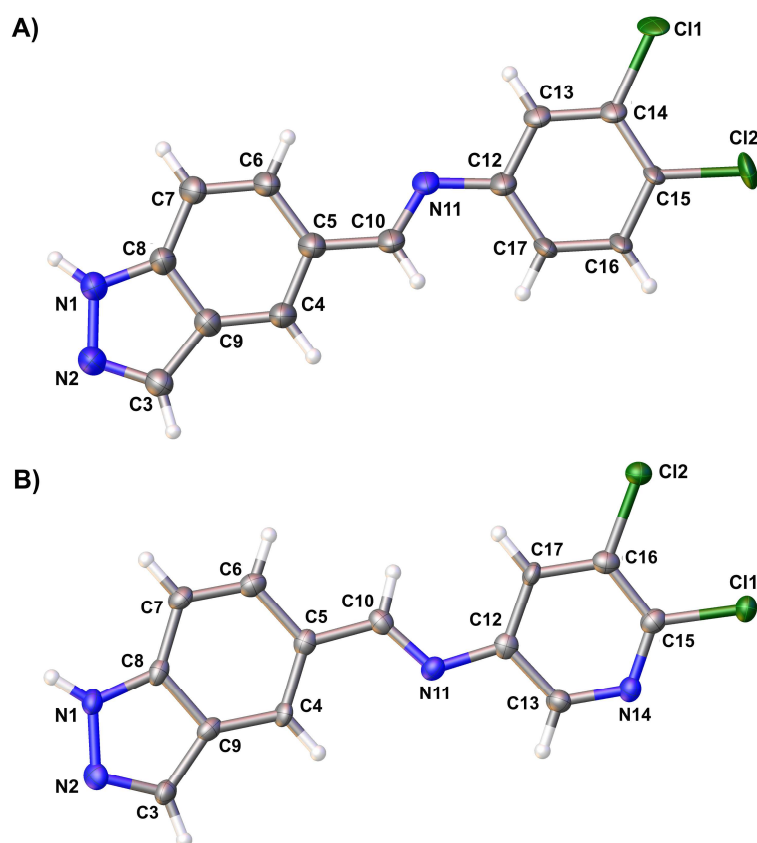


**Fig. 6.** Single X-ray structures of the major occupied part of compounds **17** (A) and **20** (B) showing the atom numbering. The thermal ellipsoids are drawn at the 50% probability level.

For compound **17**, the X-ray structure determination reveals serious disorder, however, we decided to consider the major occupied part (85%) in our docking experiments. Single crystals of **20** were twinned with a ratio of 62:38, both domains were taken into account for data integration and refinement. In both crystal structures, the two fused five- and six-membered rings of the indazole unit are nearly coplanar to the benzene respectively pyridine ring, defined the mean plane angle amounts to  $2.7(2)^\circ$  in **17** and  $7.5(2)^\circ$  in **20**. In comparison, the indazole plane and the phenyl ring plane are tilted by  $3.67(3)^\circ$  and  $6.01(5)^\circ$  in **11** and **15**, respectively (Fig. S5). The aromatic and indazole units are connected by a methanimine linkage with torsions (C5-C10-N11-C12) of  $-177.9(5)^\circ$  (in **17**) and  $-177.2(6)^\circ$  (in **20**). The angles are  $123.4(5)^\circ$  (C5-C10-N11) and  $118.1(5)^\circ$  (C10-N11-C12) for **17**, and for compound **20** respectively  $122.8(6)^\circ$  (C5-C10-N11) and  $121.0(5)^\circ$  (C10-N11-C12). The plane defined by the methanimine linker (C5, C10, N1, C12) encloses an angle of  $15.6(5)^\circ$  with the indazole moiety and an

angle of  $18.3(5)^\circ$  with the phenyl ring for **17**. For **20**, the plane defined by the methanimine linker encloses an angle of  $8.3(4)^\circ$  with the indazole moiety and an angle of  $10.6(6)^\circ$  with the pyridine unit.

Because of the lack of a carboxamide function able to build N-H...O hydrogen bridges compared to **11** and **15**, only anti-parallel double chains (hydrogen bridging) can be found between the N1-H1 and N2 atoms generated by a two-fold screw axis with N-H...N distances of 2.18(1) Å for **17** and **20**, respectively (Fig. S6). Due to the carboxamide function of subclass I compounds, intermolecular hydrogen bonds for **11** and **15** can be found between H1 and O1 formed by translation along the *b* axis forming chains with H...O distances of 2.07(2) Å in **11** and 2.17(3) Å in **15** [39]. The X-ray data for **17** and **20** point toward the importance of the indazole moiety within the observed conformation to build geometrically sound intermolecular interactions, which are relevant for MAO inhibition.

Moreover, the X-ray analysis of **17** and **20** indicates that the high MAO-B inhibitory activity of *N*-unsubstituted (indazole-5-yl)methanimines (subclass II) is due to their stable 1*H*-indazole tautomeric forms within an energetically more favourable *trans*-isomerism (*E*-isomers) (see also Section 2.5 and Supporting Information). Similar results were obtained for the tautomerism of *N*-unsubstituted indazole-5-carboxamide derivatives [39,52].

#### 2.4.2. Docking of compounds **14**, **15**, **20** and **21** into hMAO-B

Docking experiments were performed with the human model of the MAO-B enzyme. SAR evaluation of compounds reported herein, including the single X-ray analysis of carboxamides **11** and **15** [39] as well as their methanimine analogs **17** and **20**, provided valuable information about the putative binding modes of both subclass I and II compounds within the active site of hMAO-B. To find a plausible explanation for their high hMAO-B inhibitory potency, computational experiments of carboxamide derivatives with the lowest (subclass I compound **14**) and the highest hMAO-B affinity (compound **15**) were performed utilizing the crystal structure of hMAO-B (PDB code: 2V5Z) [53]; these were compared with the best docking poses for the respective methanimine analogs, e.g., subclass II compounds **20** and **21**.

Following our previously established single X-ray/molecular modeling approach [39,54], we investigated binding situations and estimated the most significant interactions and desolvation effects within *h*MAO-B. At first, binding proposals were computed with LeadIT [55]. Then, the obtained poses were used for further optimization, as well as semi-quantification of binding and visualization of the best-computed solutions using the free energy approximation "HYDE", as embedded in SeeSAR (see Experimental Section and Supporting Information) [56]. Based on our previous experiences [39], the single X-ray structure geometries (i.e., bond lengths and angles) of carboxamides **11** and **15** as well as methanimines **17** and **20** were used for docking studies. The results obtained from the molecular modeling studies provided insight and rationalization the structural features of both subclass I and II compounds in relation to: (i) the observed preference in inhibitory potency at *h*MAO-B of 3,4-dichlorophenyl- versus 5,6-dichloropyridine substituents (**15** and **21** vs. **14** and **20**), on the one hand side, and carboxamides (subclass I compounds) versus methanimines (subclass II) on the other, (ii) investigation of the hydrophobic effects including enthalpic and entropic binding, (iii) the proposed binding modes of compounds under study within the substrate cavity region of *h*MAO-B, and (iv) further exploration of subclass II compounds as CNS drugs.

It must be noted that given the overall property arrangement in the binding pocket of *h*MAO-B [hydrophobic "substrate cavity" (close to FAD)]–[hydrophilic "linker region" (on the front of the amide or methanimine linker)]–[hydrophobic "entrance cavity" (around PRO102 and 104 and PHE103)] and the close-to-symmetric complementarity of the ligands poses emerged with either the di-halogenated phenyl- or pyridine-ring pointing *towards* the FAD cofactor (Fig. 7).

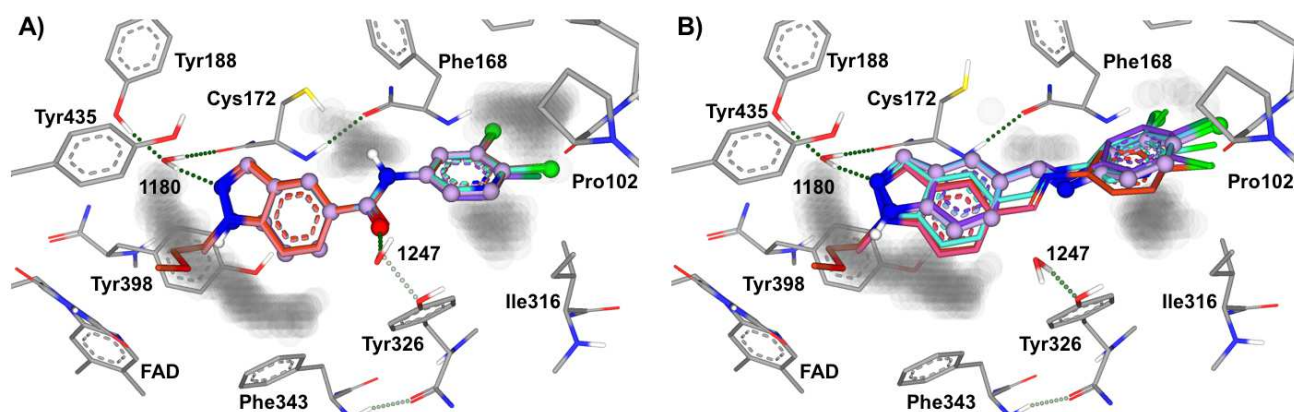


**Fig. 7.** Overlay representing the overall binding modes of carboxamides **11–16** (A, subclass I compounds) and methanimines (B, subclass II compounds) **17–22** onto the crystal structure of *h*MAO-B (PDB: 2V5Z) with the unoccupied space in the binding site (grey "fog"). The most important protein residues, water molecules (1180 and 1247) and FAD co-factor are displayed. The same color schema is used for each ligand in its analog in both subclasses. The respective parent compounds **11** and **17** are given in magenta.

The re-assessment of the X-ray structure geometries of **11** and **15** with SeeSAR resulted in a similar conformation of all subclass I compounds **11–16** within *h*MAO-B. In all carboxamides, the amide linker is rotated by 180° around the C12–N11–C10–C5 torsion angle (cp. Fig. S5). The overlay of the proposed binding modes of **11–16** clearly shows that there are no differences in their orientation within the crystal structure of *h*MAO-B (cp. Fig. 7A). In contrast, the X-ray analysis of the geometries of **17** and **20** led to two favorable conformations of methanimines **17–22** – structures that resulted from a rotation around the C12–N11–C10–C5 torsion angle (i.e., the imine linker) of about 180° (cf. Fig. 6). However, after docking, the binding modes of methanimines **17–22** show similar orientations within the active site of *h*MAO-B as their carboxamide analogs (Fig 7B).

In general, the modeling proposes the formation of a strong intermolecular H-bond between the indazole N2 and water 1180 in all compounds. This H-bond was almost the same in distance in carboxamides **14** and **15** (N2---HOH1180  $\approx$  1.9 Å); in **20** and **21** it was approximately 1.8 Å and 1.9 Å, respectively. The carboxamide linker in **14** and **15** is suggested to play an essential role as a hydrophilic anchor (i.e., H-bond acceptor/donor) for the conformation of the compounds within the substrate cavity

region of *h*MAO-B [39], interacting favorably with water molecule 1247 (for **14** and **15**: CO---HOH1247  $\approx$  1.8 Å) (see Fig. 8A). Because of the inherently missing functionalities of the methanimine linker, such a second H-bond cannot exist in subclass II compounds **20** and **21** (cf. Fig. 8B).

Furthermore, the binding modes and estimated affinities strongly suggest that the *N*-unsubstituted derivatives **14** and **20**, as well as the N1-methylated derivatives **15** and **21** occupy the same substrate cavity space, provided that the ligands investigated herein do not covalently bind with the FAD cofactor. Compounds **15** and **21** differ from **14** and **20** by the phenyl residue (instead of di-chloro-substituted pyridine) and the methyl substitution at N1. However, their binding poses show the same orientation of the indazole moiety within the "substrate cavity" region close to FAD, i.e., around the TYR398, 435 and 188 and HOH1180. The 5,6-dichloropyridine or 3,4-dihalo-substituted phenyl ring of the ligands occupies a strongly hydrophobic binding pocket of *h*MAO-B dominated by hydrophobic amino acids such as LEU164 and 167, PRO102 and 104, and isoleucin residues (cf. Fig. 7A). In addition, the computed binding models suggest that for both subclass I and II compounds the relevant N2---HOH1180 bond is highly coordinated also by protein residues CYS172 and TYR188, whereas for carboxamide derivatives **14** and **15** the water molecule HOH1247 is surrounded by GLN206, ILE199, TYR201 and 326. We conclude that the observed H-bonds are essential for the ligand stabilisation of carboxamides (CO---HOH1247), and that the conformations of all ligands (N2---HOH1180) in the binding site of *h*MAO-B are realized through non-covalent interactions.

Given the previously discussed *a priori* possibility of a flipped binding mode that results in similar total free energy estimations [39], we nonetheless favor the displayed poses in which the 5,6-dichloropyridine- (in **14** and **20**) or 3,4-dichlorophenyl-ring (in **15** and **21**) point *toward* FAD for three reasons: (i) in the safinamide co-crystal structure (2V5Z), the fluorine atom occupies the same area as the halogens in the herein discussed compounds, and (ii) the HOH1180 and 1247 were shown before to play a pivotal role on the front of FAD and, (iii) the central moiety may act as an amide linker in this orientation – also contributing to a good agreement with the estimated binding affinities.

### 2.4.3. HYDE visual free energy assessment of compounds **14**, **15**, **20** and **21**

In accordance with previous studies on related compounds [39], we also performed HYDE analyses of the new compounds in order to gain insight into the *overall* binding thermodynamics, aiming at explaining the observed differences in their inhibitory potency in *h*MAO-B (e.g., **14** and **20** vs. **15** and **21**). The HYDE scoring function as embedded in SeeSAR considers the free energy by computing the difference between the unbound and bound states. H-bonds (approximate enthalpy) and dehydration ("desolvation", approximate entropy) effects of all non-hydrogen/heavy atoms (HA), contributing to the *overall* Gibbs free energy ( $\Delta G$ ) are computed with respect to their accessibility to water before and after binding [57,58]. Both the protein (Rec) and the ligand (Lig) energy terms are considered for calculation of the respective partial contribution to the overall  $\Delta G$  of each non-hydrogen atom (Fig. 8 and Table S5).

In this HYDE study, we were particularly interested on the estimation and visualization of the major ligand-receptor interactions and desolvation effects at (i) the aromatic part of the molecules (3,4-dichlorophenyl- vs. 5,6-dichloropyridine-substitution) and (ii) the respective linker (e.g., carboxamide vs. methanimine function). Since the indazole-binding site of the pocket is spatially limited by the FAD cofactor, we analyzed the contribution of the N1-methyl substituent in **15** and **21** to the overall  $\Delta G$  compared to the *N*-unsubstituted derivatives **14** and **20**, respectively (cp. Fig. 8C and 8D). The desolvation effects for both chlorine atoms at pyridine C5 and C6 in 5,6-dichloropyridine-substituted compounds **14** and **20** (desolvation of about  $-15$  kJ/mol) is compensated by a desolvation "penalty" at pyridine nitrogen for both ligands ( $\sim 2.6$  kJ/mol for **14** and  $\sim 1.3$  kJ/mol for **20**) resulting in a HYDE contribution of the 5,6-dichloropyridine residues of about  $-18$  and  $-21$  kJ/mol for **14** and **20**, respectively (cp. Fig. 8A and 8B). In the case of 3,4-dichlorophenyl-substituted compounds **15** and **21**, the sum of the desolvation effects for both chlorine atoms at phenyl C3 and C4 positions is approximately  $-16$  (for **15**) and  $-15$  kJ/mol (for **21**), leading to a partial HYDE score for the 3,4-dichlorophenyl substituent of about  $-21$  and  $-20$  kJ/mol for **15** and **21**, respectively.

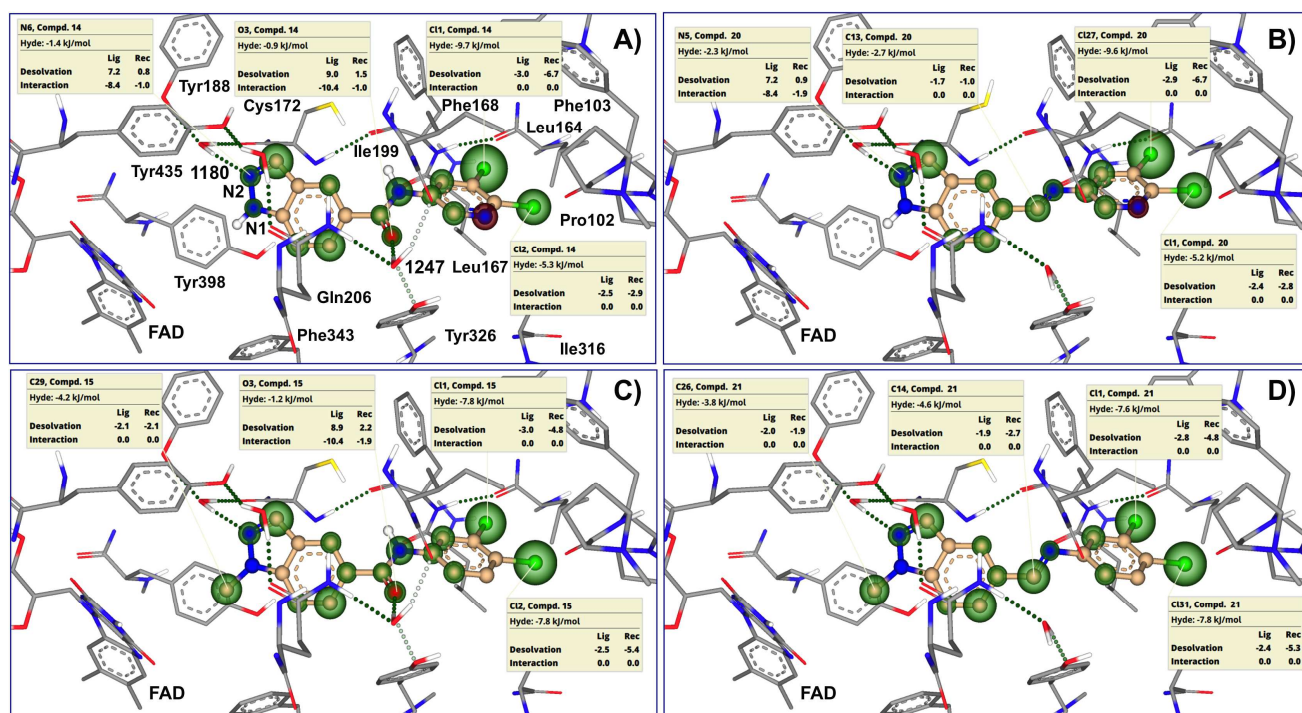


**Fig. 8.** SeeSAR visualization of binding of the *N*-unsubstituted compounds **14** (A) and **20** (B) and *N*1-methylated analogs **15** (C) and **21** (D) to the crystal structure of the *h*MAO-B-safinamide complex (PDB: 2V5Z) with HYDE quantification of the most important non-hydrogen atoms contributing to the binding affinities (binding free energies  $\Delta G$ ) of compounds. HYDE visual affinity assessment: green = favorable, red = unfavorable and non-colored = no relevant for affinity. For clarity, the most important protein residues, water molecules (1180 and 1247) and FAD co-factor are shown in the same orientation, color code and structure representation as in Fig. 8.

With exception of compound **14** that exhibits the lowest predicted *h*MAO-B potency (i.e., approximately  $-3$  kJ/mol lower than calculated for **20**), there is no major difference between the 5,6-dichloropyridine in **20** and the 3,4-dichlorophenyl residues in **15** and **21**, when comparing their partial contribution to the total free binding energy. Further HYDE analyses provide similar contributions of the most important HA to the free energy for the investigated compounds, including the amide spacers in **14** and **15** (e.g., N11, C10, and O1) and imine atoms (C10 and N11) in **20** and **21**, respectively (see Figs. S5 and 7). As mentioned above, the flexible carboxamide linkage between two lipophilic moieties in the indazole-5-carboxamides (subclass I) is crucial not only for the observed high MAO-B inhibitory potency (NH-C(=O) contribution of  $\sim 4.8$  and  $5.0$  kJ/mol for **14** and **15**, respectively), but also acts as an ‘anchor’ in the more hydrophobic parts in the pocket [39]. However, our HYDE analysis provides hints

toward why there is similar (or even better for **14** vs. **20**) *h*MAO-B affinity of methanimine compounds **20** and **21** compared to their carboxamide analogs **14** and **15**: There are "coronas" at their imine nitrogen and also favorable contributions at the ether C10 atom (see Fig. 9).

Furthermore, the N1-indazole methyl group in **15** and **21** occupies the hydrophobic FAD-subpocket favorably – yielding a HYDE contribution of approximately  $-4$  kJ/mol in each molecule. The N1-methylated compounds (**15** and **21**) exhibit significant preferences towards the *h*MAO-B enzyme compared to the *N*-unsubstituted compounds (**14** and **20**) due to their higher entropic contributions (corresponding to desolvation effects) to the total binding energy of both lipophilic parts, comprising the 3,4-dichlorophenyl ring and the N1-indazole methyl group. In the case of both N1-methylated compounds (**15** vs. **21**), the additional H-interaction (enthalpic effect) at the carbonyl function (e.g., CO--HOH1247) in **15** did not show a higher contribution to the overall binding energy when compared to the imine linker in **21** (NH-C=O) contribution of  $\sim 5.0$  kJ/mol vs.  $\sim 5.3$  kJ/mol of the N=CH linker). The sum of the desolvation effects for the 3,4-di-Cl-Ph ring and the N1-methyl group in **15** ( $-25.2$  kJ/mol) is marginally higher than those in **21** ( $-23.2$  kJ/mol). The HYDE analyses of compounds **14**, **15** and **20**, **21** reproduced their *h*MAO-B activities, which decrease as follows: **15** ( $IC_{50} = 0.386$  nM,  $\Delta G = -45.6$  kJ/mol) > **21** ( $IC_{50} = 1.03$  nM,  $\Delta G = -43.6$  kJ/mol) > **20** ( $IC_{50} = 1.28$  nM,  $\Delta G = -41.4$  kJ/mol) > **14** ( $IC_{50} = 5.42$  nM,  $\Delta G = -38.7$  kJ/mol).

Finally, we computed the estimated affinities of our compounds (**11–22**) in SeeSAR (SeeSAR's HYDE reports  $K_i$  ranges rather than values to avoid an overinterpretation of affinity estimation) at all biological targets of interest (e.g., *h*MAO-A, *h*MAO-B, *h*AChE and *h*BuChE) (Fig. S7). All final poses of the compounds were validated (with  $N = 5$  poses after docking) and visually inspected. Reassuringly, for *h*MAO-B, the selected poses lie in the respective affinity regions – as confirmed by biological experiments. However, it should be mentioned that against *h*MAO-A and *h*ChEs these compounds were inactive and, therefore, no enzyme kinetics were performed. Overall, there is a good agreement with the estimated affinity ranges for compounds under study at *h*MAO-B, e.g., HYDE scores ( $K_i$  HYDE ranges in

the low nM range) /  $K_i$  values (in the (sub-)nM area) (cf. Fig. S7B and Table 1). Consistently, the N1-substitution in **15** and **21** appears to be more favorable for *h*MAO-B inhibition ( $K_i = 0.17$  and  $0.46$  nM for **15** and **21** vs.  $2.39$  and  $0.57$  nM for **14** and **20**).

In conclusion, the results obtained from the docking studies and HYDE analyses suggested that (i) an imine linker is well-tolerated by *h*MAO-B; it has a similar contribution to the total binding energy in methanimines **17–22** as the amide linker in **11–16**, (ii) a replacement of the amide or imine linker by other electron rich groups will also be favorable for *h*MAO-B inhibition, and (iii) considering the optimal substituent length of four atoms, a large hydrophilic substitution should make the indazole N1 position less accessible for water, leading to an improvement of affinity toward *h*MAO-B or other relevant targets because the desolvation penalty upon binding should be smaller. We esteem these findings to be crucial for future design of CNS drug.

### 2.5. Profiling of physicochemical properties

In the course of our comparative study we further analyzed the photophysical properties of carboxamide **11** (subclass I compounds) and selected methanimines (subclass II compounds **17** and **20**), as well as the drug-like profile of all compounds **11–22** and reference safinamide. Due to the specific physicochemical properties of Schiff bases (compounds **17–22**), we performed further examination of **17** and **20** with focus on: (i) chemical stability and photosensitivity, and (ii) possible isomer (*E/Z*-isomerism and tautomerism) formation and distribution by using of time- and solvent-dependent photophysical experiments (UV-Vis), LC/ESI-MS analysis and quantum-chemical calculations.

#### 2.5.1. Photophysical evaluation

Electronic absorption spectra of **11**, **17** and **20** were measured in different solvents, including dry DMSO, acetonitrile (ACN) and methanol (MeOH) at a concentration of  $50 \mu\text{M}$  (Table 3). The UV-Vis spectra of carboxamide **11** exhibited different profile compared to those of both methanimines **17** and **20** due to the linker-specific absorbance features of chromophores (e.g., amide vs. imine linker) (see Fig.

S8). The absorption maxima ( $\lambda_{\max}$ ) of **11** were found to be 265 (in DMSO) and ~262 nm (in ACN and MeOH), while for **17** and **20** the  $\lambda_{\max}$  values lie in the range of 300–325 nm. Compared to **11** and **17**, compound **20** exhibits higher  $\lambda_{\max}$  at the same experimental conditions due to its pyridine moiety. The largest differences in the absorption maxima between **11** and methanimines **17** ( $\lambda_{\max}$  ~322 nm) and **20** ( $\lambda_{\max}$  = 325 nm) were observed to be 54 nm for **11** vs. **17** and 57 nm for **11** vs. **20**, respectively (cp. Table 3). Furthermore, the compounds showed slight differences in their molar absorptivity ( $\epsilon$ ) measured in the respective solvents. For all compounds, the molar absorptivities decrease with increasing the solvent polarity, with the lowest  $\epsilon$  values observed for methanimines **17** and **20** in methanol.

In addition, the UV-Vis experiments of **11**, **17** and **20** show that no solvent-dependent absorption changes, neither in polar aprotic conditions (e.g., DMSO and ACN as solvent) nor in methanol, could be observed. Therefore, the UV-Vis spectra suggest that under these experimental conditions (i) carboxamide **11** as well as methanimines **17** and **20** exist in their most stable single tautomeric 1*H*-indazole form and (ii) no structural changes (e.g., hydrolysis) of **17** and **20** could be detected (cp. Fig. S8, for details, see Supporting Information). These results were confirmed by quantum-chemical calculations performed with the uncharged possible tautomeric forms of **17** and **20** (cp. Section 2.5.2).

In order to further investigate the chemical stability of methanimine-based Schiff bases subjected in this work, time-dependent stability experiments in different solvents with compound **20** were performed (Fig. S9). For this purpose, samples of **20** (at 50  $\mu$ M) in DMSO, ACN or MeOH were exposed to daylight for 76 days at ambient temperature and the UV-Vis absorption spectra measured across the time (Fig. S9A–S9C). The single and superposition UV-Vis spectra of the corresponding building blocks, e.g., 1*H*-indazole-5-carbaldehyde (**2**) and 5,6-dichloropyridin-3-amine (**6**), measured at 50  $\mu$ M in MeOH/H<sub>2</sub>O 1:1 were used as reference (Fig. S9D).

**Table 3** Photophysical data of compounds **11**, **12**, **17**, and **20** (at 50  $\mu$ M) in different solvents.<sup>a</sup>

Compd.	DMSO		ACN		MeOH	
	$\lambda_{\max}^b$	$\epsilon^c$	$\lambda_{\max}^b$	$\epsilon^c$	$\lambda_{\max}^b$	$\epsilon^c$
<b>11</b>	267.5	19426	262.5	19023	262	18486
<b>17</b>	321.5	19042	300	19168	312.5	17627
<b>20</b>	325	15334	313.5	18124	314.5	15063

<sup>a</sup> All measurements were performed at  $25.0 \pm 0.01^\circ\text{C}$ . <sup>b</sup> Unit: nm. <sup>c</sup> Unit:  $\text{M}^{-1}\text{cm}^{-1}$ . na = not applicable.

In the experiments with **20** in polar aprotic solvents, no spectral changes can be detected across the time of 76 days, suggesting that no degradation of **20** occurs in DMSO and ACN and, therefore, these solvents can be used for preparation of stock solutions of methanimines under study (compounds **17**–**22**). In contrast, the experiments with **20** in methanol clearly showed a decrease of the absorption maxima accompanied by changes of the absorbance spectra, indicating that a slow degradation of **20** is occurring over time (cp. Fig. 9C and 9E). Furthermore, we observed that **20** was stable during the first 3 days under these conditions, while a gradually hydrolysis (~68%) of **20** was occurred after 76 days in methanol (cp. Fig. S8F).

As next, we investigated the ability of imine **20** to undergo a photo-induced [2+2]-cycloaddition (dimerization) as well as its concentration-dependent stability using different samples of the compound in dry methanol (1.0 and 10 mM). The samples were then exposed to daylight at ambient temperature for certain period of time, slowly evaporated either to dryness or to a minimum solvent and analyzed by LC/ESI-MS or X-ray structural analysis. The results are depicted in Figure S10. In these experiments, we observed that the imine **20** was relatively stable during the first 24–96 hours at both test concentrations (1.0 and 10 mM). Only traces of a dimer of **20** were detected by LC/ESI-MS after 96 hours in methanol (at 1.0 mM). Compound **20** was found to be stable under these conditions, while a slow hydrolysis of **20** was occurred after 62 days (Fig. S10A–10C). Crystallization of **20** was observed when its sample (10 mM) was kept for 43 hours and slowly evaporated to a minimum solvent (Fig. S10D and S10F). The structure of crystalline **20** was confirmed by X-ray crystal analysis (cp. Figure 7). Altogether, the stability experiments demonstrated that the imine **20** is chemically stable and non-

photosensitive for up to 96 hours in diluted as well as concentrated methanol solutions. In polar aprotic solvents such as DMSO and ACN, compounds **17** and **20** are completely stable.

Moreover, the results obtained from the chemical stability and photosensitivity experiments suggested that the imines **11–22** are relatively stable under the experimental conditions used in this work, thus offering further opportunities for structural modifications. However, there are some limitations to consider. It is known that a fast hydrolysis of imines could be observed in water/alcohol mixtures and/or under acidic conditions, in which the degradation rate depends on the water/alcohol ratio. Therefore, it appears to be indispensable to avoid the use of different alcoholic solutions for performing test samples of these compounds, especially for long-term experiments.

#### 2.5.2. Evaluation of *E/Z* isomerism and tautomerism

For a better understanding of the relationship between the bioactivity at the configurational ground state (e.g., *E* vs. *Z* isomers) and the isomeric stability of (indazole-5-yl)methanimines **17–22**, the respective *E/Z*-geometry and possible tautomeric forms of compounds **17** and **20** was studied by means of quantum-chemical calculations [59]. The *E/Z*-isomers for both compounds formed via a rotation of the respective 3,4-dichloro-phenyl (for **17**) and 5,6-dichloro-pyridine ring (for **20**) around the methanimine linker are illustrated in Figure S11. The possible tautomers (tautomeric indazole forms **a–c**) of **17** and **20** are sketched in Fig. S12, while the relative energies of their isomers and conformers in gas phase and different solvents are collected in Table S7 and S8, respectively (see Supporting Information).

The theoretical calculations were performed using the M06-2X functional [60] with TZVP basis set [61]. This fitted hybrid meta-GGA functional with 54% Hartree-Fock (HF) exchange has been specially developed to describe main-group thermochemistry and non-covalent interactions; it has previously shown very good results for the prediction of tautomeric equilibrium compounds with intramolecular hydrogen bonds [62]. Solvent effects are described by using the Polarizable Continuum Model (the integral equation formalism variant, IEFPCM) [63].

Lowest energy geometries for the corresponding conformers and pertinent molecular parameters, such as the equilibrium energy  $E$  (in Hartree), were calculated for **17-1E-a** and **20-1E-a** isomers (see Tables S7 and S8). It is worth mentioning that  $E$ -isomers arising from rotation around the N–C<sub>Ph</sub> single bond are equally probable (**17-1E-a/17-1E-b** and **20-1E-a/20-1E-b**). The molecular planes, i.e., indazole vs. 3,4-dichloro-phenyl or 5,6-dichloro-pyridine ring, are not planar, which is a typical behavior of the Schiff bases and confirms the proposed binding modes of **17** and **20** within the *h*MAO-B binding site [64]. The bond angle between the indazole and the phenyl moiety in **17-1E-a** (C<sub>Ind</sub>–C=N–C<sub>Ph</sub>) or the pyridine residue in **20-1E-a** (C<sub>Ind</sub>–C=N–C<sub>Pyr</sub>) in different solvents are  $-141^\circ$  or  $-139^\circ$ , respectively (Fig. S11). For Schiff bases such angle is typically in the range between  $-140^\circ$  and  $-160^\circ$ . For both compounds, the  $E$ -isomeric form is energetically more favorable compared to the  $Z$ -isomer. The energy differences are large enough to conclude that latter should be presented neither in gas phase nor in solution under the assumption of the PCM solvent model.

The studied compounds are potentially tautomeric. The possible tautomers of **17** and **20** are shown in Figure S12. However, according to the theoretical calculations the respective tautomeric forms **b-d** are energetically unfavorable and should not be presented in solution. The results arising from the calculations in different solvents as well as in gas phase suggested that there is no tautomeric equilibrium for methanimines **17** and **20** (cp. Tables S7 and S8). Compounds **17** and **20** exist in their most stable *1H*-indazole tautomers **a** (e.g., **17-1E-a** and **20-1E-a**), which are confirmed by NMR and X-ray analysis (Fig. 10). Furthermore, each of these tautomers exists as a mixture of all together four rotamers, as a consequence of rotation around the imine C=N and the C<sub>ind</sub>–C<sub>imine</sub> bonds. Interestingly, for each compound **17** and **20** two most stable tautomeric forms **1E-a** and **2E-a** were estimated. For both imines **17** and **20**, there is about 3.84 kcal/mol difference between the most stable rotamers of tautomers **1E-a** and **2E-a** in water as solvent (Fig. 9), suggesting that the studied compounds exist as single tautomers in solution. Similar results were obtained for both compounds in gas phase and MeOH, ACN, and DMSO as solvents (cf. Table S7 and S8).

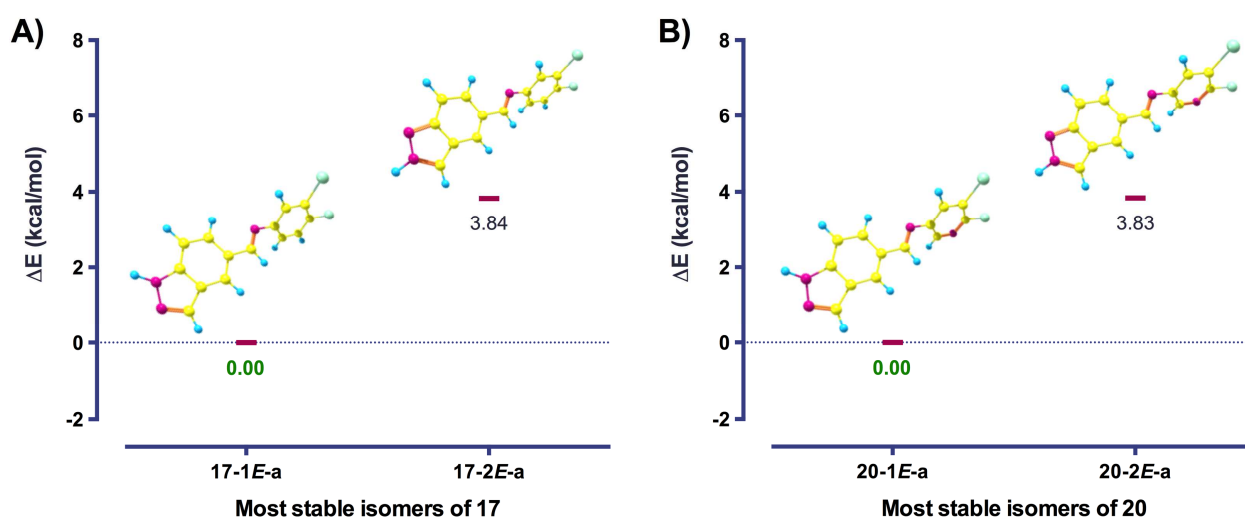


**Fig. 9.** Energy diagram representing the calculated most stable tautomers of compounds **17** (A) and **20** (B) in water, presented as most stable *E*-isomers. Similar results were obtained for calculations in gas phase, methanol, acetonitrile, and DMSO (for details, see Table S7 and S8).

Overall, our results from the quantum-chemical and photophysical analysis of **17** and **20** indicate that the high inhibitory potency and selectivity of the MAO-B inhibitors reported herein due to their *1H*-indazole tautomeric form, which is in agreement with the results obtained from the molecular modeling experiments. Moreover, based on quantum-chemical calculations, it can be further concluded that (indazole-5-yl)methanimines **17–22** exist in their more favorable *E*-isomeric form, allowing formation of rotamers through a rotation of the *di*-halo-substituted phenyl or pyridine ring around the imine linker. Compared to the carboxamide linker in **11–16**, the imine spacer in **17–22** allows also greater flexibility within the active site of *h*MAO-B.

### 2.5.3. Evaluation of drug-likeness

Due to the specific requirements for early development of CNS drugs, the relevant drug-like and physicochemical properties of compounds **11–22** and reference IMAO-B safinamide (SAF) were subsequently estimated (Table 4). The calculated drug-likeness and physicochemical parameters included: hydrogen bond acceptor and donor (HBA and HBD) counts [65], number of rotatable bonds (RotB) [65], topological surface area (*t*PSA) [66], percent absorption (%ABS) [48], blood (plasma)-

brain partition coefficient ( $\log_{BB}$ ) [67], aqueous solubility at pH 7.4 (expressed as  $\log_{S_{7.4}}$ ), distribution coefficient at pH 7.4 ( $\log_{D_{7.4}}$ ), and ligand-lipophilicity efficiency (LLE) [68,69].

The most relevant properties are within the suggested limits for oral bioavailability and penetration into the central nervous system (CNS+ drugs:  $MW \leq 400$ ,  $HBA \leq 7$ ,  $HBD \leq 3$ ,  $RotB < 8$ , and  $tPSA < 70 \text{ \AA}^2$ ) [66–43], similar to those observed for safinamide (Table 4). The *N*-unsubstituted carboxamides (subclass I compounds **11–14**) and the majority of the imines (subclass II compounds **17–20**) have molecular weight that is lower ( $MW < 300 \text{ Da}$ ) or close to the one of the reference drug safinamide ( $MW 302 \text{ Da}$ ). To predict the oral bioavailability of compounds under study, we estimated their percentage absorption (%ABS), which depends on the topological polar surface area ( $tPSA$ ) that is used for calculation of %ABS [39,48]. All compounds have  $tPSA$  values below  $60 \text{ \AA}^2$ , indicating that they are expected to be orally bioavailable ( $\%ABS \geq 60\%$ ) and thus classified as good brain penetrable ( $tPSA < 60\text{--}70 \text{ \AA}^2$ ) CNS candidates [40,67,67,69]. Furthermore, we also calculated the blood(plasma)-brain partition coefficients ( $\log_{BB}$ ) of all compounds in order to initially predict their BBB permeability [67]. All compounds in Table 4 exhibit a  $\log_{BB} > -1$  indicating a possible BBB permeability [66]. With exception of the *N*-unsubstituted imines **17–20**, the remaining compounds exhibited higher  $\log_{BB}$  values than safinamide ( $\log_{BB} = -0.09$ ).

The aqueous solubility (expressed as  $\log_{S}$ ) and distribution coefficient ( $\log_{D}$ ) at physiological pH 7.4 reveal a slightly preferable solubility-lipophilicity balance for carboxamides **11–16** over imines **17–22**. As expected, the lowest  $\log_{S_{7.4}}$  values were calculated for the most lipophilic derivatives in both subclasses (carboxamides **15, 16** and imines **21, 22**), exhibiting *N*-alkyl substituents at the indazole N1 position. The calculated  $\log_{D_{7.4}}$  values are in the range 3–5, being above the optimal scope 1–4 for CNS drugs [70]. The ligand-lipophilicity efficiency (LLE), a multiparameter metric that is often used for evaluation of a drug candidate, for all carboxamides **11–16** and imine **20** was found to be in the optimal range ( $5 < LLE < 7$ ) [40,71]. A good correlation between bioactivity and oral bioavailability was observed when plotting the most important parameters, including biological affinity ( $pIC_{50}$  values at

*h*MAO-B), lipophilicity values ( $\text{clogD}_{7.4}$ ), molecular weight (MW), *t*PSA, and aqueous solubility values ( $\text{logS}_{7.4}$ ), for all compounds as well as the reference inhibitor safinamide (Fig. 10). With the exception of carboxamide **16**, all other compounds matched the respective targeted areas (green squares). Overall, the estimated drug-like properties were in line with the general requirements (e.g., rule-of-5) for drug-likeness of CNS drug candidates [71]. However, it appears evident that (indazole-5-yl)methanimines **17–22** (subclass II) exhibit higher lipophilicity and, subsequently, possessed lower solubility and smaller LLE values than their carboxamide analogs **11–16** (subclass I compounds).

**Table 4.** Physicochemical and drug-like properties of compounds **11–22** and safinamide (SAF)

Compd.	MW	pIC <sub>50</sub>	HBA/D <sup>a</sup>	RotB <sup>a</sup>	<i>t</i> PSA <sup>a</sup>	%ABS <sup>b</sup>	logBB <sup>a</sup>	logS <sub>7.4</sub> <sup>a</sup>	logD <sub>7.4</sub> <sup>a</sup>	LLE <sup>c</sup>
<b>11</b>	306	9.23	2/2	2	57.8	89.1	0.065	-4.56	3.73	5.50
<b>12</b>	290	9.17	2/2	2	57.8	89.1	0.030	-4.49	2.99	6.18
<b>13</b>	290	9.18	2/2	2	57.8	89.1	0.030	-4.49	2.99	6.19
<b>14</b>	307	8.27	3/2	2	70.7	84.6	-0.067	-4.58	2.93	5.34
<b>15</b>	320	9.41	2/1	2	46.9	92.8	0.246	-4.82/-5.45 <sup>d</sup>	3.76/3.24 <sup>e</sup>	5.65/6.17
<b>16</b>	364	8.97	3/1	5	56.2	89.6	0.159	-4.79	3.69	5.28
<b>17</b>	290	9.21	2/1	2	41.0	94.9	-0.159	-4.72	4.61	4.60
<b>18</b>	274	8.68	2/1	2	41.0	94.9	-0.261	-4.67	3.84	4.84
<b>19</b>	274	8.72	2/1	2	41.0	94.9	-0.261	-4.67	3.84	4.88
<b>20</b>	291	8.89	3/1	2	53.9	90.4	-0.445	-4.66	3.60	5.29
<b>21</b>	304	8.99	2/0	2	30.2	98.6	0.213	-5.00	4.74	4.25
<b>22</b>	348	8.89	3/0	5	39.4	95.4	0.130	-4.96	4.67	4.22
<b>SAF</b>	302	8.29	3/2	7	64.3	86.8	-0.090	-4.22	2.89	5.40
<sup>f</sup> CNS+	≤400	>8	≤7/≤3	<8	<60–70	≥60	≥-1	≥-5.0	1–4	>5

MW, molecular weight; HBA/D, number of hydrogen bond acceptors/donors; *t*PSA, topological surface area (in Å<sup>2</sup>); RotB, number of rotatable bonds; SAF, Safinamide. <sup>a</sup> Properties calculated using the StarDrop module in SeeSAR [56]. <sup>b</sup> %ABS: % of absorption = 109 - 0.345 × *t*PSA. [48,66] <sup>c</sup> LLE: ligand-lipophilicity efficiency = pIC<sub>50</sub> - logD<sub>7.4</sub>. <sup>d</sup> Solubility (in mol/L) measured at pH 7.4 in 60 mM phosphate buffer, at rt. <sup>e</sup> Distribution coefficient measured at pH 7.4 in 60 mM phosphate buffer, at rt. <sup>f</sup> CNS+: required ranges for compound's penetration into the CNS [65,66,69,70].

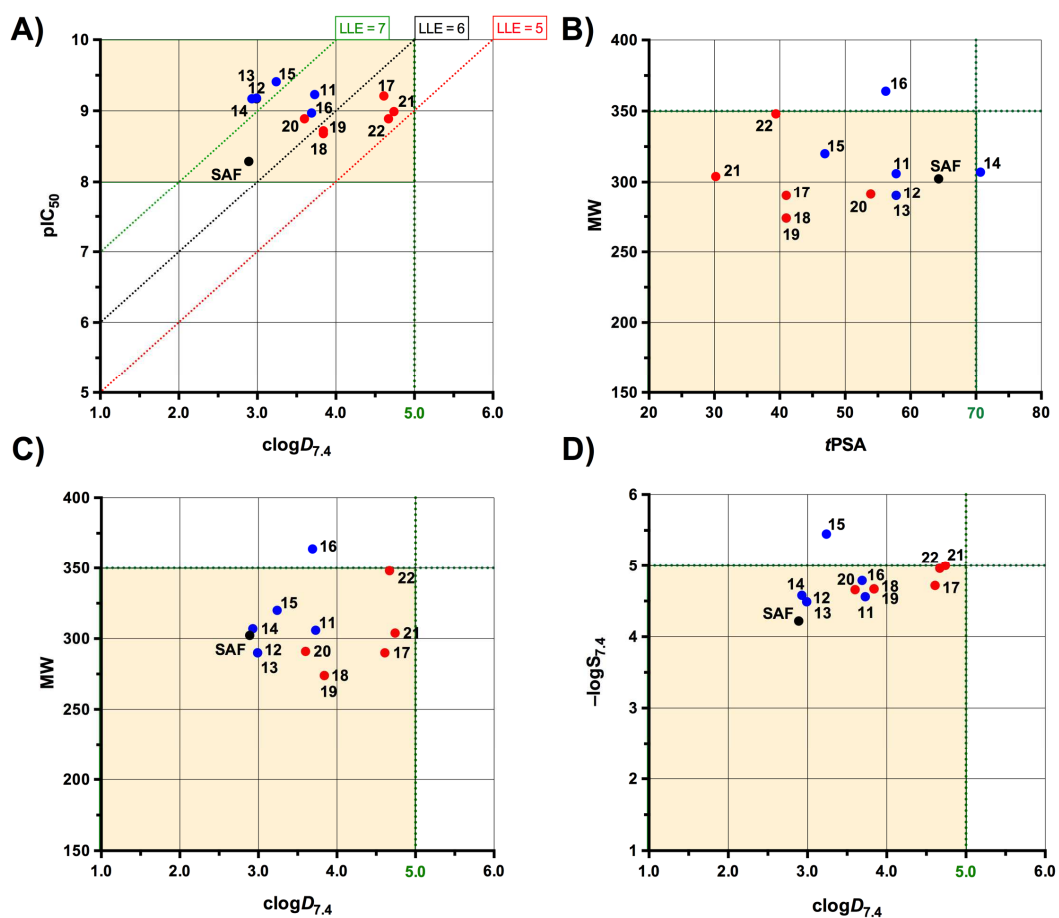


**Fig. 10.** Distribution of physicochemical properties of reference safinamide (SAF), indazole-5-carboxamides **11–16** (blue circles, subclass I compounds) and (indazole-5-yl)methanimines **17–22** (red circles, subclass II compounds): (A) Square plot of potency ( $\text{pIC}_{50}$  at *h*MAO-B) vs.  $\text{cLogD}_{7.4}$  values representing an excellent lipophilic ligand efficiency ( $\text{LLE} \geq 5$ ) for all compounds under study, (B) Square plot of molecular weight (MW in Da) vs.  $t\text{PSA}$  (in  $\text{\AA}^2$ ), (C) Square plot of molecular weight (MW in Da) vs.  $\text{cLogD}_{7.4}$ , and (D) Square plot of aqueous solubility ( $-\log S_{7.4}$ ) vs.  $\text{cLogD}_{7.4}$ . The green dashed lines represent the preferred ranges (green squares) for  $\text{pIC}_{50}$  ( $\geq 8.0$ ),  $\text{cLogD}_{7.4}$  ( $\leq 5.0$ ),  $t\text{PSA}$  ( $< 70 \text{\AA}^2$ ), MW ( $\leq 350$  Da), and  $-\log S_{7.4}$  ( $\leq 5.0$ ).

## 2.6. Pan Assay Interference compounds (PAINS) screening

Due to the chemical structure of subclass II compounds **17–22** (e.g., methanimine-based Schiff-bases), artificial activity of all compounds was evaluated both theoretically (free available tools) and experimentally (time- and solvent-dependent photophysical studies). Compounds under study were investigated whether they are PAINS or colloidal aggregators by using different *in silico* tools (for details, see Supporting Information) [72]. The biological tests suggested that our compounds are

inactive on rat and human MAO-A isoform and, therefore, they cannot be considered as false positive inhibitors. Furthermore, compounds did not absorb light or fluorescence in a region used to measure MAO inhibitory activity ( $>570$  nm), so that they are not interfering with the assay. In addition, the selective inhibition of *h*MAO-B, determined by some most active inhibitors, was evaluated as a reversible and competitive process. The results of all theoretical tests are in agreement with the experimental data suggesting that our compounds are non-PAINS molecules and did not act as aggregators. In addition, the selective *h*MAO-B inhibitors reported herein have not shown artificial activities under the experimental conditions used for their biological and photophysical evaluation.

### 3. Conclusion

In conclusion, we have performed a comparative study of structurally related indazole-5-carboxamide (subclass I compounds **11–16**) and (indazole-5-yl)methanimine (subclass II **17–22**) derivatives, including screening toward human MAO-B and MAO-A, as well as human AChE and BuChE inhibition, preliminary investigation of hepatotoxicity, molecular modeling studies including desolvation-aware scoring, photochemical stability, and evaluation of drug-likeness. In general, SAR analysis suggested that the compounds investigated herein are selective and potent inhibitors of human MAO-B with  $IC_{50}$  values ranging from low nanomolar to even picomolar potency (*h*MAO-B). The N1-methylated compounds **15** (*h*MAO-B  $IC_{50} = 0.386$  nM,  $K_i = 0.17$  nM, SI = 25907) and **21** (*h*MAO-B  $IC_{50} = 1.03$  nM,  $K_i = 0.46$  nM, SI = 9709) act as competitive and reversible IMAO-B. Moreover, both indazole N1-methylated derivatives were found to be the only compounds in both series possessing selective inhibitory activity in the moderate  $\mu$ M range against *h*AChE isoform. Furthermore, compounds **11** and **17** demonstrated no risk of drug-induced hepatotoxicity, as determined by preliminary hepatotoxicity screening in human hepatocarcinoma HepG2 cells. To explain their high MAO-B affinity, the binding mode of selected indazole-5-carboxamide versus (indazole-5-yl)methanimine derivatives within the binding pocket of the *h*MAO-B enzyme was investigated. For

this purpose, we implemented a well-validated modeling platform using the single X-ray structures of selected imines **17** and **20**. Moreover, we inserted the free energy approximation concept "HYDE" to estimate, visualize and quantify the effects of (de)hydration and hydrogen bonding. The data of molecular modeling indicate the existence of an imine linker is well-tolerated by *h*MAO-B, leading to a similar contribution to the total binding energy in methanimines **17–22** as the amide spacer in **11–16**. Photophysical experiments under different conditions supported by quantum-chemical calculations suggested that the imines **17–22** exhibited the required photochemical stability and exist as *1H*-indazole tautomers in their more favorable *E*-isomer forms, thus offering further opportunities for structural modifications. Overall, the estimated drug-like properties were in line with the general requirements for drug-likeness of CNS drug candidates. Future efforts will be directed toward further structural modifications and optimizations of imine analogs with regard to physicochemical profile, chemical and metabolic stability, multi-target activity, and toxicity.

## 4. Experimental section

### 4.1. Chemistry

#### 4.1.1. General methods

All commercially available anhydrous solvents, reagents, starting materials, and reference compounds were obtained from various producers (Acros, Sigma-Aldrich, Alfa Aesar, Key Organics, Sigma-Aldrich, TCI, and VWR) and used without purification or drying unless otherwise noted. Dry *N,N*-dimethylformamide (DMF, 99.8% extra dry over molecular sieves, AcroSeal, Acros) was used throughout the synthesis. Ampuwa water-for-injection (WFI, Fresenius Kabi) was applied for preparation of different methanol-water mixtures. Reactions were routinely monitored by thin layer chromatography (TLC) on pre-coated silica gel plates and visualized using UV light (Merck 60 F<sub>254</sub>, 230–400 mesh). Preparative column chromatography was performed on Acros Organics silica gel 60Å (Sigma-Aldrich/Merck 60, 0.063-0.200 mm, 70–230 mesh ASTM). The organic layer obtained after extraction from aqueous phases was dried over anhydrous sodium sulfate. Solvents were removed *in vacuo* on a Büchi Rotavapor R-100/R-300. Mass spectra were recorded on an API 2000 mass spectrometer (electron spray ion source ESI, Applied Biosystems) coupled with an Agilent 1100 HPLC system (see Supporting Information). NMR spectra were recorded on a Bruker Avance 500 MHz spectrometer. Melting points are uncorrected and were measured on a Büchi B545 apparatus. The <sup>1</sup>H and <sup>13</sup>C NMR spectra were recorded at room temperature (303 K) using DMSO-*d*<sub>6</sub> as a solvent. Chemical shifts ( $\delta$ ) are reported in parts per million (ppm) relative to the residual solvent peak in the corresponding spectra: DMSO-*d*<sub>6</sub>  $\delta$  2.50 (<sup>1</sup>H) and 39.51 (<sup>13</sup>C). Coupling constants *J* are given in Hertz (Hz), and spin multiplicities are given as singlet (s), broad singlet (br s), doublet (d), doublet of doublets (dd), doublet of doublets of doublets (ddd), triplet (t), doublet of triplets (dt), quartet (q), and multiplet (m). The purity of all final products was found to be not less than 95% by LC/ESI-MS analyses. Commercially available 1*H*-indazole-5-carboxylic acid (**1**, Sigma-Aldrich) and 1*H*-indazole-5-

carboxaldehyde (**2**, Sigma-Aldrich) were used as starting materials for the preparation of the *N*-alkyl-substituted carboxylic acids (**7** and **8**) and *N*-alkyl-substituted carbaldehydes (**9** and **10**), respectively. The analytical data of 1-(2-methoxyethyl)-1*H*-indazole-5-carboxylic acid (**8**) were reported previously [39]. The experimental procedure and spectroscopic analysis for the *N*-methoxyethyl-substituted carbaldehyde **10** are provided in the Supporting Information. Compounds **11–13** and **15** are commercially available (Key Organics, Camelford, UK). Compound **14** was prepared using revised procedures, and for this, the analytical data is reported in the Experimental Section.

#### 4.1.2. General procedure A for the preparation of compounds **11–16**

A solution of the respective 1*H*-indazole-5-carboxylic acid or 1-alkyl-1*H*-indazole-5-carboxylic acid (**1** or **7**, **10**, 1.0 mmol), 3,4-dichloroaniline or 5,6-dichloropyridin-3-amine (**3–5** or **6**, 1.1–1.2 mmol), *N*-ethyl-*N'*-(3-dimethylaminopropyl)carbodiimide hydrochloride (EDC-HCl, 1.0–1.2 mmol) in methanol (5.0 mL) was stirred over night at room temperature. The reaction was then poured into water (10 mL), stirred for 30 min at room temperature, filtered, washed with water (3 × 10 mL), and then dried at 70 °C. The crude product was purified by column chromatography on silica gel (mobile phase: dichloromethane/MeOH 9/1 v/v) following by recrystallization from petroleum ether/dichloromethane.

##### 4.1.2.1. *N*-(5,6-dichloropyridin-3-yl)-1*H*-indazole-5-carboxamide (**14**)

Off-white-greyish solid (125 mg, 93%); mp >290 °C (dec.). <sup>1</sup>H NMR (500 MHz, DMSO-*d*<sub>6</sub>) δ = 7.67 (d, *J* = 8.82 Hz, 1H, Ph), 8.05 (d, *J* = 8.51 Hz, 1H, Ph), 8.21 (s, 1H, Ind.-Het.), 8.34 (s, 1H, Pyr.), 8.44 (s, 1H, Ph), 8.74 (s, 1H, Pyr), 12.8 (s, 1H, CONH), 13.55 (s, 1H, NH). <sup>13</sup>C NMR (125 MHz, DMSO-*d*<sub>6</sub>) δ = 110.1, 111.1, 120.5, 123.0, 123.2, 123.9, 126.3, 126.7, 127.1, 135.3, 136.1, 141.4, 163.1. ESI-MS (*m/z*): calcd. for C<sub>13</sub>H<sub>8</sub>Cl<sub>2</sub>N<sub>4</sub>O: 306.008; found 305.121 [M – H]<sup>–</sup>, 307.301 [M + H]<sup>+</sup>.

#### 4.1.3. General procedure B for the preparation of compounds **17–22**

A solution of the corresponding 1*H*-indazole-5-carbaldehyde (**2**), 1-methyl-1*H*-indazole-5-carbaldehyde (**9**) or 1-(2-methoxyethyl)-1*H*-indazole-5-carbaldehyde (**10**) (1.0 equiv.), different

substituted anilines **3–6** (1.1 equiv.) and acetic acid (0.1 mL/mmol, pH 4–5) in ethanol (3.0 mL/mmol) was stirred under reflux until a precipitation took place. After cooling to room temperature, the reaction mixture was sonicated until complete precipitation. The precipitate formed was filtered and dried at 70 °C. The crude product was purified by column chromatography on silica gel (mobile phase: dichloromethane/MeOH 9/1 v/v) and recrystallized three times from petroleum ether/dichloromethane.

#### 4.1.3.1. (*E*)-*N*-(3,4-dichlorophenyl)-1-(1*H*-indazol-5-yl)methanimine (**17**)

White solid (258 mg, 90%); mp 207.1–207.5 °C. <sup>1</sup>H NMR (500 MHz, DMSO-*d*<sub>6</sub>) δ = 7.27 (dd, *J* = 2.52 / 8.51 Hz, 1H, Ph), 7.55 (d, *J* = 2.53 Hz, 1H, Ph), 7.63 (s, 1H, Ph), 7.65 (s, 1H, Ph), 8.12 (dd, *J* = 1.26 / 8.83 Hz, 1H, Ph), 8.24 (s, 1H, Ind.-Het.), 8.29 (s, 1H, Ph), 8.73 (s, 1H, CH=N), 13.35 (s, 1H, NH). <sup>13</sup>C NMR (125 MHz, DMSO-*d*<sub>6</sub>) δ = 110.9, 122.1, 122.7, 123.0, 125.1, 125.2, 127.7, 128.9, 131.1, 131.7, 135.2, 141.5, 151.9, 163.2. ESI-MS (*m/z*): calcd. for C<sub>14</sub>H<sub>9</sub>Cl<sub>2</sub>N<sub>3</sub>: 289.017; found 288.051 [M – H]<sup>–</sup>, 290.270 [M + H]<sup>+</sup>.

#### 4.1.3.2. (*E*)-*N*-(3-chloro-4-fluorophenyl)-1-(1*H*-indazol-5-yl)methanimine (**18**)

White solid (107 mg, 69%); mp 171.9–172.6 °C. <sup>1</sup>H NMR (500 MHz, DMSO-*d*<sub>6</sub>) δ = 7.29 (ddd, *J* = 2.52/4.41/8.83 Hz, 1H, Ph), 7.44 (t, *J* = 8.83 Hz, 1H, Ph), 7.52 (dd, *J* = 2.52/6.62 Hz, 1H, Ph), 7.64 (d, *J* = 8.83 Hz, 1H, Ph), 8.02 (dd, *J* = 1.26/8.83 Hz, 1H, Ph), 8.23 (s, 1H, ind-het), 8.27 (s, 1H, Ph), 8.72 (s, 1H, CH=N), 13.33 (s, 1H, NH). <sup>13</sup>C NMR (125 MHz, DMSO-*d*<sub>6</sub>) δ = 110.9, 117.3 (d, *J* = 21.69 Hz), 120.0 (d, *J* = 18.7 Hz), 122.2 (d, *J* = 7.23 Hz), 122.5, 123.0, 125.0 (d, *J* = 19.94 Hz), 128.9, 135.2, 141.4, 149.0 (d, *J* = 3.24 Hz), 154.4, 156.4, 162.6. ESI-MS (*m/z*): calcd. for C<sub>14</sub>H<sub>9</sub>ClFN<sub>3</sub>: 273.047; found 272.032 [M – H]<sup>–</sup>, 274.261 [M + H]<sup>+</sup>.

#### 4.1.3.3. (*E*)-*N*-(4-chloro-3-fluorophenyl)-1-(1*H*-indazol-5-yl)methanimine (**19**)

White solid (158 mg, 58%); mp 198.7–199.2 °C. <sup>1</sup>H NMR (500 MHz, DMSO-*d*<sub>6</sub>) δ = 7.15 (ddd, *J* = 1.26/2.52/8.51 Hz, 1H, Ph), 7.37 (dd, *J* = 2.2/10.72 Hz, 1H, Ph), 7.59 (t, *J* = 8.52 Hz, 1H, Ph), 7.64 (d, *J* = 8.83 Hz, 1H, Ph), 8.02 (dd, *J* = 1.26/8.83 Hz, 1H, Ph), 8.24 (s, 1H, ind-het), 8.28 (s, 1H, Ph), 8.73 (s,

1H, CH=N), 13.35 (s, 1H, NH). <sup>13</sup>C NMR (125 MHz, DMSO-*d*<sub>6</sub>) δ = 109.4 (d, *J* = 21.45 Hz), 110.9, 116.1 (d, *J* = 17.95 Hz), 119.0 (d, *J* = 2.74 Hz), 123.0, 125.1 (d, *J* = 8.33 Hz), 128.8, 130.9, 135.2, 141.5, 152.6 (d, *J* = 7.97 Hz), 156.7, 158.6, 163.1. ESI-MS (*m/z*): calcd. for C<sub>14</sub>H<sub>9</sub>ClFN<sub>3</sub>: 273.047; found 272.032 [M – H]<sup>–</sup>, 274.271 [M + H]<sup>+</sup>.

#### 4.1.3.4. (*E*)-*N*-(5,6-dichloropyridin-3-yl)-1-(1*H*-indazol-5-yl)methanimine (**20**)

Yellow solid (52 mg, 65%); mp 236.9–238.4 °C. <sup>1</sup>H NMR (500 MHz, DMSO-*d*<sub>6</sub>) δ = 7.66 (d, *J* = 8.51 Hz, 1H, Ph), 8.02 (dd, *J* = 1.26/8.83 Hz, 1H, Ph), 8.14 (dd, *J* = 2.20 Hz, 1H, Ph), 8.26 (s, 1H, ind-het), 8.31 (s, 1H, Pyr), 8.36 (d, *J* = 2.52 Hz, 1H, Pyr), 8.82 (s, 1H, CH=N), 13.38 (s, 1H, NH). <sup>13</sup>C NMR (125 MHz, DMSO-*d*<sub>6</sub>) δ = 111.0, 123.0, 125.1, 125.6, 128.6, 129.3, 130.9, 135.4, 141.6, 141.8, 143.6, 148.1, 165.4. ESI-MS (*m/z*): calcd. for C<sub>13</sub>H<sub>8</sub>Cl<sub>2</sub>N<sub>4</sub>: 290.013; found 289.051 [M – H]<sup>–</sup>, 291.220 [M + H]<sup>+</sup>.

#### 4.1.3.5. (*E*)-*N*-(3,4-dichlorophenyl)-1-(1-methyl-1*H*-indazol-5-yl)methanimine (**21**)

Light yellowish solid (275 mg, 91%), mp: 145.7–146.2 °C. <sup>1</sup>H NMR (500 MHz, DMSO-*d*<sub>6</sub>) δ = 4.09 (s, 3H, N1Me), 7.28 (dd, *J* = 2.53 / 8.52 Hz, 1H, Ph), 7.56 (d, *J* = 2.53 Hz, 1H, Ph), 7.63 (s, 1H, Ph), 7.65 (s, 1H, Ph), 7.75 (dd, *J* = 0.63 / 8.83 Hz, 1H, Ph), 8.05 (dd, *J* = 1.58 / 8.83 Hz, 1H, Ph), 8.22 (d, *J* = 0.94 Hz, 1H, Ind.-Het.), 8.28 (s, 1H, Ph), 8.74 (s, 1H, CH=N). <sup>13</sup>C NMR (125 MHz, DMSO-*d*<sub>6</sub>) δ = 35.7, 110.5, 122.1, 122.7, 123.6, 125.0, 125.3, 125.2, 127.8, 128.9, 131.1, 131.7, 134.2, 141.1, 151.8, 163.0; ESI-MS (*m/z*): calcd. for C<sub>15</sub>H<sub>11</sub>Cl<sub>2</sub>N<sub>3</sub>: 303.033; found 302.140 [M – H]<sup>–</sup>, 304.120 [M + H]<sup>+</sup>.

#### 4.1.3.6. (*E*)-*N*-(3,4-dichlorophenyl)-1-(1-(2-methoxyethyl)-1*H*-indazol-5-yl)methanimine (**22**)

White solid (72 mg, 66%); mp 228.8–229.4 °C. <sup>1</sup>H NMR (500 MHz, DMSO-*d*<sub>6</sub>) δ = 3.18 (s, 3H, OMe), 3.77 (t, *J* = 5.36 Hz, 2H, CH<sub>2</sub>), 4.60 (t, *J* = 5.36 Hz, 2H, NCH<sub>2</sub>), 7.28 (ddd, *J* = 1.58/2.52/8.51 Hz, 1H, Ph), 7.56 (t, *J* = 2.31 Hz, 1H, Ph), 7.65 (dd, *J* = 1.58/8.52 Hz, 1H, Ph), 7.78 (d, *J* = 8.83 Hz, 1H, Ph), 8.03 (d, *J* = 8.83 Hz, 1H, Ph), 8.24 (d, *J* = 0.63 Hz, 1H, ind-het), 8.27 (s, 1H, Ph), 8.73 (s, 1H, CH=N). <sup>13</sup>C NMR (125 MHz, DMSO-*d*<sub>6</sub>) δ = 48.5, 58.2, 70.7, 110.8, 122.1, 122.7, 123.6, 125.0, 125.2,

127.7, 128.9, 131.1, 131.7, 134.7, 141.4, 151.9, 163.0. ESI-MS ( $m/z$ ): calcd. for  $C_{17}H_{15}Cl_2N_3O$ : 347.059; found 348.180  $[M + H]^+$ .

## 4.2. Biological experiments

### 4.2.1. Monoamine oxidase inhibition assays

Assay of monoamine oxidase inhibitory activities of compounds under study on human MAO-A and -B isoforms were performed as previously described [38,39] using a continuous fluorescence-based method [43,44]. The following stock solutions were used: test compounds (10 mM) in DMSO (1.0% final concentration), reference MAO inhibitors (0.5 mM), *p*-tyramine (100 mM), and resorufin sodium salt (2.0 mM) in deionized water. Briefly, MAO inhibition was determined using commercially available recombinant human MAO-A and MAO-B enzymes expressed in baculovirus-infected insect cells (BTI-TN-5B1-4, Sigma-Aldrich, M7316 and M7441). *p*-Tyramine was used as a substrate in a final concentration of 150  $\mu$ M for the human MAO assays. For performing the MAO assays, the commercial MAO assay kit Amplex<sup>®</sup> Red (Thermo Fisher Scientific Inc., USA) was used. The samples with the test compounds together with the respective amounts of human MAO-A/MAO-B were incubated for 20 min at 37°C (pH 7.4) with Amplex Red reagent, reconstituted horseradish peroxidase (HRP), and the respective amount of *p*-tyramine. Clorgyline and selegiline (each in a final concentration of 1.0  $\mu$ M) were used as positive controls for both human MAO-A and MAO-B assay, respectively. Fluorescent measurements were performed for 45 min and the concentration-response curves of the reference inhibitors clorgyline (MAO-A) and selegiline (MAO-B) served as positive controls for both rat and human MAO assays. A sample with DMSO (2.0  $\mu$ L) served as a negative control. The inhibition of MAO enzymes was measured with at least two initial concentrations (10 and 0.1  $\mu$ M) followed by determination of full inhibition curves of the respective active compound. Human MAO inhibition assays were performed in triplicate in 96-well plates (200  $\mu$ L final volume) by measuring the effects of

the tested compounds (*in situ* formation of a fluorescent derivative resorufin) on the production of hydrogen peroxide (H<sub>2</sub>O<sub>2</sub>) obtained from *p*-tyramine.

#### 4.2.2. Data analysis of monoamine oxidase assays

The IC<sub>50</sub> values were determined by non-linear regression analysis of MAO inhibition versus the logarithm (–log) of the tested compound molar concentration and calculated by mean IC<sub>50</sub> value ± SEM (standard error of the mean) of at least three independent experiments ( $n \geq 3$ ). For the calculation of the respective  $K_i$  values, the Cheng-Prusoff equation [45] was used as follows:  $K_i = IC_{50} (1 + [S]/K_m)$ , where [S] is the substrate concentration and  $K_m$  its concentration required to reach half-maximal velocity (Michaelis constant,  $V_{max}/2$ ).

#### 4.2.3. Evaluation of hMAO-B enzyme kinetics

The steady-state kinetic parameters ( $K_m$ , Michaelis constant and  $V_{max}$ , maximum velocity rate) of the enzymatic activity of the hMAO-B enzyme were determined under the experimental conditions described above [39] by an oxidative deamination reaction of the substrate *p*-tyramine (0.12–1.0 mM). In our experiments, hMAO-B displayed a Michaelis constant ( $K_m$ ) of  $118.8 \pm 1.23 \mu\text{M}$  with a maximal velocity ( $V_{max}$ ) of  $40.4 \pm 1.13 \text{ nmol } p\text{-tyramine}/\text{min per mg protein}$  ( $n = 3$ ).

#### 4.2.4. Evaluation of the type of hMAO-B inhibition

The type of binding of compounds **15** and **21** (final concentrations of 1.0 nM) and the reference inhibitors selegiline (30 nM, irreversible, Irr) and safinamide (50 nM, reversible, Rev) to hMAO-B enzyme was determined by time-dependent inhibition experiments with modification of previously reported protocols [47]. The tested compounds and the reference inhibitors were studied at their IC<sub>80</sub> values without pre-incubation of the hMAO-B enzyme/inhibitor mixtures. Control experiments without inhibitors were run simultaneously for each compound and experiment. The enzyme reaction was started by adding 10  $\mu\text{M}$  of the substrate *p*-tyramine and the enzymatic activity of the tested compounds was measured for 20 min. Then, the substrate concentration was increased to 1.0 mM final

concentration of *p*-tyramine and the enzyme reactivation was monitored for a 300 min period. Determination of the enzymatic activity was performed as described above for the *h*MAO-B assay. The percentage of *h*MAO-B enzyme activity (% of control) was plotted against the incubation time to evaluate the time-dependent enzyme inhibition. Data are the mean  $\pm$  SD ( $n = 4$ ).

#### 4.2.5. Evaluation of mechanism of *h*MAO-B inhibition

The mechanism of *h*MAO-B inhibition of the representative compounds **15** and **21** was evaluated in substrate-dependent kinetic experiments. Catalytic rates of *h*MAO-B were measured at five different concentrations of the substrate *p*-tyramine (0.05–1.5 mM) in the absence (no inhibitor) or presence of three different concentrations of **14** (0.5, 1.0 and 5.0 nM). The results are presented as double reciprocal Lineweaver-Burk plots ( $1/V$  vs.  $1/[p\text{-tyramine}]$ ) and the corresponding non-linear saturation curves ( $V$  vs.  $[p\text{-tyramine}]$ ). The experiments were conducted using the same *h*MAO-B assay conditions as described above for the determination of *h*MAO enzyme activity. Data are the mean  $\pm$  SD ( $n = 3$ ).

#### 4.2.6. Evaluation of cholinesterase inhibitory activity

The inhibition of cholinesterase enzymes (*h*AChE and *h*BuChE) was determined based on Ellman's method [73] with slight modifications, as previously reported [41,42]. The assay solution was prepared by mixing 50  $\mu$ L of Tris-HCl buffer (50 mM, pH 8 containing 0.1% BSA) with 125  $\mu$ L of 5,5'-dithiobis(2-nitrobenzoic acid) (DTNB, 3.0 mM in 50 mM Tris-HCl, pH 8 containing 0.1 M NaCl and 0.02 M  $\text{MgCl}_2 \times 6\text{H}_2\text{O}$ ), 25  $\mu$ L of 0.05 U/mL acetylcholinesterase from human erythrocytes (Sigma Aldrich) or 0.05 U/mL of butyrylcholinesterase from human serum (Sigma-Aldrich) as sources for human AChE or BuChE, respectively. Then, 25  $\mu$ L of each test sample at different concentrations were added to the solution and pre-incubated with the respective enzyme for 10 minutes at 37°C. The reaction was started by adding 25  $\mu$ L of acetylthiocholine iodide (5.0 mM) or *S*-butyrylthiocholine iodide (5.0 mM) as the substrate for *h*AChE or *h*BuChE, respectively. The absorbance was measured at 405 nm for 15 minutes with UV/Vis microplate spectrophotometer. Samples were evaluated at different

concentrations (100, 50, 25, 10, 1.0, and 0.1  $\mu\text{M}$ ). Galantamine hydrobromide was used as a positive control in both cholinesterase assays. Both cholinesterase assays were performed in the absence of the respective enzyme and, therefore, these samples were used as a negative control. Results are expressed as percentage of inhibition or  $\text{IC}_{50}$  and compared with those of galantamine. The % of inhibition for each test compounds was calculated as follows:

$$\% \text{ Inhibition} = ((A_{\text{sample}} - A_{\text{negative control}}) \times 100 - 100)^{-1}$$

Where  $A_{\text{sample}}$  and  $A_{\text{negative control}}$  are the measured absorption of the respective test sample and those of the negative control. Data are the mean  $\pm$  SD ( $n = 3$ ).

#### 4.2.7. Cytotoxicity evaluation

##### 4.2.7.1. Preparation of cell cultures

Human hepatocellular carcinoma cells (HepG2; ECACC, UK) were cultured in Dulbecco's modified Eagle's medium (DMEM, Gibco, Austria) supplemented with 10% fetal bovine serum (FBS; Gibco, Austria), penicillin (100 U/mL) and streptomycin (0.1 mg/mL) solution (Gibco, USA). All cells were cultured under a humidified  $\text{CO}_2$  (5.0%) atmosphere at  $37^\circ\text{C}$  and passaged by trypsinization when reached approximately 80% confluence. For experiments, cells in exponential phase of growth (at a density of 5,000 cells/well) were seeded into 96-well flat-bottom plates after treatment with trypsin-EDTA (Greiner, Germany) solution at a final volume of 100  $\mu\text{L}$ /well. Cells were incubated overnight before treatment with test substances.

##### 4.2.7.2. Cell viability assay

The cytotoxicity of compounds **11** and **17** was evaluated in HepG2 cells by colorimetric assay using 3-(4,5-dimethylthiazol-2-yl)-2,5-diphenyltetrazolium bromide (MTT) as a dye reagent. The MTT reduction assay was used to estimate the decrease in mitochondrial dehydrogenase activity in cells exposed to the test compounds and compared to the control group. In the assay, the yellow tetrazolium salt (MTT) is reduced in viable cells to insoluble purple formazan crystals, which were later dissolved in

a lysine solution. After incubation time, the cells were treated with the test compounds at different concentrations (0.1, 1.0, 2.0, 5.0, 10, 25, and 50  $\mu\text{M}$ ) and further incubated for 72 h at 37°C. Stock solutions of the compounds (10 mM) in DMSO were used to prepare test samples with a final DMSO concentration of 0.1%, which did not interfere with the cells' viability. After incubation period, MTT solution was added and cells were incubated for further 3.5 hrs. Then, the medium was removed and the plates were placed in a plate shaker at room temperature until complete dissolution of purple formazans. The quantification of formazans produced from the biological sample after reduction of MTT was monitored using a microplate ELISA reader (BioTek, USA) at a wavelength of 550 nm with a reference wavelength of 630 nm. The cytotoxicity of the test compounds determined by MTT assay was expressed as percentage cell viability according to the following equation:

$$\% \text{ Cell viability} = (A_{\text{sample}} - A_{\text{blank}}) / (A_{\text{control}} - A_{\text{blank}}) \times 100$$

Where  $A_{\text{sample}}$ ,  $A_{\text{blank}}$  and  $A_{\text{control}}$  are the measured absorption of the respective test sample, blank solution and control sample. Data are the mean  $\pm$  SD ( $n = 4$ ).

### 4.3. Crystallography

Crystals for X-ray structure analysis were grown from acetonitrile (1.5–2.0 mL) for **17** or methanol (1.0 mL) for **20** by slowly evaporation of the solvent at room temperature. Single crystals were obtained directly from their mother liqueur containing minimum solvent (0.2–0.3 mL). The crystal data were collected on a Rigaku Oxford Diffraction diffractometer with Atlas detector using  $\text{Cu K}\alpha$  radiation. The crystals were kept at 100.0 K during data collection. The structures were solved and refined with the ShelX [74] program package using direct methods and least-squares minimization. All non-hydrogen atoms were refined anisotropically. Hydrogen atoms bound to nitrogen and all hydrogen atoms in **9** were refined isotropically, other hydrogen atoms were placed in calculated positions and refined using a riding model. For molecular graphics Olex2 [75] program was used. Detailed information for X-ray analysis, crystallographic data and refinement results of compounds **17** and **20** are given in the Supporting information.

CCDC 1915450 (**17**) and CCDC 1915449 (**20**) contain the supplementary crystallographic data for this paper. These data can be obtained free of charge from The Cambridge Crystallographic Data Centre via [www.ccdc.cam.ac.uk/data\\_request/cif](http://www.ccdc.cam.ac.uk/data_request/cif).

#### 4.4. Molecular modeling studies

##### 4.4.1. Ligand and protein preparation

For docking experiments, the crystal X-ray structures of **17** and **20** were chemically valid and thus used as input without any further preparation. As recently reported for our docking purposes, the X-ray crystallographic structure exhibited an excellent agreement between experiment and re-docking computation, better than the optimized (MMFF94x force field) 3D structures of **17** and **20** [39]. The 3D structures of all other ligands were built on the basis of either the single X-ray structure of **11** and **15** (for carboxamides **11–16**) or **17** and **20** (for methanimines **18, 19, 21, and 22**) using the 3D editor in SeeSAR [56]. The crystal structure of the *h*MAO-B enzyme in complex with safinamide (PDB code: 2V5Z) [53] was obtained from the Protein Databank (PDB). For the docking experiments with the *h*MAO-B co-crystal structure, all computations were performed in the 2V5Z chain B (for details, see Supporting Information).

##### 4.4.2. Pose generation and docking

For dockings, we used FlexX docking module in LeadIT from BioSolveIT [55] applying the well-established procedure that had previously been published previously [39]. The docking algorithm in LeadIT relies on the FlexX and SIS incremental build-ups [76]. LeadIT has both accurately reproduced the experimental safinamide *binding modes* and yielded correct pose sorting of all ligands; we requested top 10 LeadIT poses for each ligand that were then re-ranked as described below. The selected best-scored poses share a large part of the safinamide pocket from the PDB 2V5Z structure. For accuracy, all poses obtained from LeadIT module were post-scored in SeeSAR (a maximum of 10 poses in the output) and the best one was selected for further discussion in this work [39].

#### 4.4.3. HYDE assessment

Post-scoring was performed with HYDE as integrated in SeeSAR from BioSolveIT [56,77]. HYDE is an atom increment system using logP values; affinity estimates are conducted using a comparison between the bound and unbound states. We refer to the citations for more details on the scoring. After HYDE computations that run for very few seconds, SeeSAR visualizes the (HYDE-) estimated free energy of binding ( $\Delta G$ ); spherical "coronas" ranging from dark red (unfavorable) to dark green (favorable for affinity) visualize the contribution of an atom and its environment to the overall free energy of binding; corona sizes correlate with the amount of contribution [78]. SeeSAR enables quick and interactive assessments of the free energy of binding and torsions [79]. Upon user demand, the software can visualize and semi-quantitatively report both protein and ligand contributions, and the split-up into entropic (desolvation/dehydration,  $-T\Delta S$ ) and enthalpic terms ( $\Delta H$ ) of  $\Delta G$ ; this enables a rough estimation of the thermodynamic profile (for details, see Supporting Information, Figure S3 and Table S5).

#### 4.4.4. Ligand ADME

Prediction of related drug-like / ADME properties of compounds under investigation was carried out using the Optibrium StarDrop [80] algorithms as interfaced in SeeSAR [56].

### 4.5. Photophysical experiments

#### 4.5.1. UV-Vis spectrophotometry

The UV-Vis spectra of compounds **2**, **6**, **11**, **12**, **17** and **20** were recorded with a Jasco V-570 UV-Vis/NIR spectrophotometer (Jasco Analytical Instruments Inc., USA) in 1.0 cm quartz cells in the interval of 200–700 nm with bandwidth of 2.0 nm and scanning speed of 100 nm/min. The concentration of the samples was 50  $\mu\text{M}$  for all compounds. The measurements were performed in different solvents at  $25.0 \pm 0.1$  °C. A blank sample with the corresponding solvent was used to calibrate the instrument. Recorded UV-Vis spectra were automatically processed and base line corrected (see

Supporting Information). The long-term solvent-dependent experiments of compound **20** were performed in dry DMSO, acetonitrile (ACN), and abs. methanol (MeOH). The respective 1.0 cm quartz cuvette was degassed with argon for 10 min., the UV-Vis spectra were immediately recorded ( $t = 0$  d) and over a period of 76 days ( $t = 76$  d) under the conditions mentioned above.

#### 4.5.2. Theoretical calculations

Quantum-chemical calculations were performed using the Gaussian 09 D.01 program suite [59]. The M06-2X density functional theory [60] was used with TZVP basis set [61]. This fitted hybrid meta-GGA functional with 54% Hartree-Fock (HF) exchange has been specially developed to describe main-group thermochemistry and non-covalent interactions; it has previously shown very good results for the prediction of tautomeric equilibrium compounds with intramolecular hydrogen bonds [62]. All structures were optimized in their ground states without restrictions in gas phase and in the indicated solvents, using tight optimization criteria and ultrafine grid in the computation of two-electron integrals and their derivatives. The true minima were verified by performing frequency calculations in the corresponding environment. Solvent effects are described by using the Polarizable Continuum Model (the integral equation formalism variant, IEFPCM, as implemented in Gaussian 09) [63]. Details for quantum-chemical calculations with compounds **17** and **20** are given in the Supporting Information.

#### 4.6. Statistics

For the MAOs enzymatic inhibition studies, the compounds were initially screened at 10  $\mu\text{M}$ , and for all, dose-response curves were built. The respective  $\text{IC}_{50}$  values were obtained by non-linear analysis. For the ChEs enzymatic inhibitory assays, the compounds were screened in the range 10–100  $\mu\text{M}$ . The respective  $\text{IC}_{50}$  values were obtained by non-linear analysis. For the cytotoxicity assay, MTT reduction for each treatment was calculated as the % of control untreated cells and plotted in column graphs ( $\pm\text{SD}$ ). Statistical comparison between the different groups was carried by one-way analysis of variance (ANOVA-1) followed by Dunnett's post-test ( $\alpha = 0.05$ , 95% confidence intervals). Differences

were considered as significant for  $p < 0.05$ . Data analysis was performed with GraphPad Prism v.6.0 software (GraphPad Software, Inc.). The results were expressed as means  $\pm$  SEM or SD for the number of independent assays ( $n = 3$  or  $4$ ) as indicated for each experiment.

### **Acknowledgments**

The authors would like to thank Dr. Sonja Hinz. N.T.T. thanks Angelika Fischer, Anika Püsche, Marion Schneider, Sabine Terhart-Krabbe, and Annette Reiner for technical assistance. N.T.T. is grateful to Nicholas Foster from Optibrium for the provision of a temporary StarDrop module license within SeeSAR.

### **Appendix A. Supplementary data**

Supplementary data related to this article can be found at <http://dx.doi.org/...>

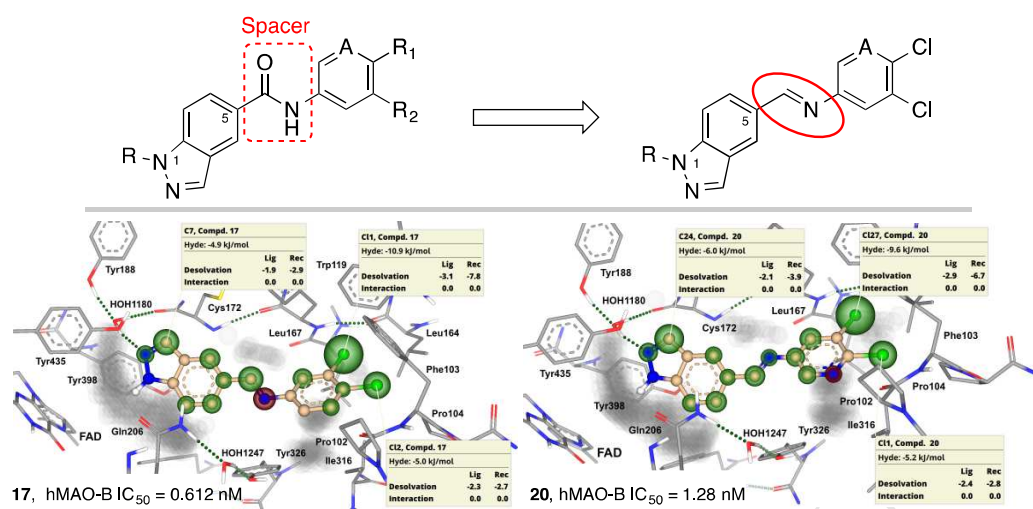
**ABBREVIATIONS USED**

ACN, acetonitrile; AD, Alzheimer's disease; ACh, acetylcholine; AChE, acetylcholinesterase; BBB, blood-brain barrier; BuChE, butyrylcholinesterase; BSA, bovine serum albumin; CHO, Chinese hamster ovary; ChE, cholinesterase; CNS, central nervous system; COMT, catechol-*O*-methyltransferase; DA, dopamine; DMF, *N,N*-dimethylformamide; DMSO, *N,N*-dimethyl sulfoxide; DDI, DOPA-decarboxylase inhibitor; ED, electron donor; EDC, *N*-ethyl-*N'*-(3-dimethylaminopropyl)carbodiimide; EDTA, ethylenediaminetetraacetic acid; ESI, electrospray ionization; FAD, flavin adenine dinucleotide; h, human; HA, heavy atom; HBA, hydrogen bond acceptor; HBD, hydrogen bonding domain; HEPES, 2-(4-(2-hydroxyethyl)-1-piperazin-1-yl)ethanesulfonic acid; HRP, horseradish peroxidase; HYDE, hydrogen dehydration; LLE, lipophilic ligand efficiency; MAO, monoamine oxidase; MMS, methyl methanesulfonate; MTT, 3-(4,5-dimethylthiazol-2-yl)-2,5-diphenyltetrazolium bromide; ND, neurodegenerative disease; PD, Parkinson's disease; PET, positron emission tomography; PNS, peripheral nervous system; PCM, Polarizable Continuum Model; r, rat; ROS, reactive oxygen species; SAR, structure-activity relationship; TLC, thin-layer chromatography.

**Notes**

MG is employee of BioSolveIT, manufacturer of one of the software packages used herein.

## TABLE OF CONTENTS GRAPHIC



**Highlights**

- A comparative study of carboxamides *vs.* methanimines as selective and reversible MAO-B inhibitors has been performed.
- (Indazole-5-yl)methanimines **17–22** exhibit similar or even higher potency against *h*MAO-B than their indazole-5-carboxamide analogs **11–16**.
- Compounds **11** and **17** showed no risk of drug-induced hepatotoxicity.

ACCEPTED MANUSCRIPT

**References**

- [1] Alzheimer's Association, 2019 Alzheimer's disease facts and figures, *Alzheimers Dement.* 15 (2019) 321–387.
- [2] J.M. Ellis, M.J. Fell, Current approaches to the treatment of Parkinson's Disease, *Bioorg. Med. Chem. Lett.* 27 (2017) 4247–4255.
- [3] K.A. Jellinger, Basic mechanisms of neurodegeneration: a critical update, *J. Cell. Mol. Med.* 14 (2010) 457–487.
- [4] M.H. Horrocks, S.F. Lee, S. Gandhi, N.K. Magdalinou, S.W. Chen, M.J. Devine, L. Tosatto, M. Kjaergaard, J.S. Beckwith, H. Zetterberg, M. Iljina, N. Cremades, C.M. Dobson, N.W. Wood, D. Klenerman, Single-molecule imaging of individual amyloid protein aggregates in human biofluids, *ACS Chem. Neurosci.* 7 (2016) 399–406.
- [5] T. Chitnis, H.L. Weiner, CNS inflammation and neurodegeneration, *J. Clin. Invest.* 127 (2017) 3577–3587.
- [6] A.K. Kakkar, N. Dahiya, Management of Parkinson's disease: Current and future pharmacology, *Eur. J. Pharmacol.* 750 (2015) 74–81.
- [7] A. Samii, J.G. Nutt, B.R. Ransom, Parkinson's disease, *Lancet* 363 (2004) 1783–1793.
- [8] T. Wang, R.G. Qui, M. Yu, Predictive modeling of the progression of Alzheimer's disease with recurrent neural networks, *Sci. Rep.* 8 (2018) 9161 1–12.
- [9] A.J. Lees, J. Hardy, T. Revesz, Parkinson's disease, *The Lancet* 373 (2009) 2055–2066.
- [10] G. Park, J. Tan, G. Garcia, Y. Kang, G. Salvesen, Z. Zhang, Regulation of histone acetylation by autophagy in Parkinson disease, *J. Biol. Chem.* 291 (2016) 3531–3540.
- [11] P.A.Q. Videira, M. Castro-Caldas, Linking glycation and glycosylation with inflammation and mitochondrial dysfunction in Parkinson's disease, *Front. Neurosci.* 12 (2018) A381.
- [12] N.T. Tzvetkov, A.G. Atanasov, Natural product-based multitarget ligands for Alzheimer's disease treatment? *Future Med. Chem.* 10 (2018) 1745–1748.

- [13] A.K. Kakkar, N. Dahiya, Management of Parkinson's disease: Current and future pharmacology, *Eur. J. Pharmacol.* 750 (2015) 74–81.
- [14] D. Aarsland, B. Creese, M. Politis, K.R. Chaudhuri, D.H. Ffytche, D. Weintraub, C. Ballard, Cognitive decline in Parkinson disease, *Nat. Rev. Neurol.* 13 (2017) 217–231.
- [15] W. Poewe, K. Seppi, C.M. Tanner, G. M. Halliday, P. Brundin, J. Volkmann, A.-E. Schrag, A.E. Lang, Parkinson disease, *Nat. Rev. Dis. Primers* 3 (2017) A17013.
- [16] R.R. Ramsay, A. Albrecht, Kinetics, mechanism, and inhibition of monoamine oxidase, *J. Neural Transm.* 125 (2018) 1659–1683.
- [17] G. Spigolon, G. Fisone, Signal transduction in L-DOPA-induced dyskinesia: from receptor sensitization to abnormal gene expression, *J. Neural Transm.* 125 (2018) 1171–1186.
- [18] P. Dunkel, C.L. Chai, B. Sperlágh, P.B. Huleatt, P. Mátyus, Clinical utility of neuroprotective agents in neurodegenerative disease: current status of drug development for Alzheimer's, Parkinson's and Huntington's diseases, and amyotrophic lateral sclerosis, *Exp. Opin. Investig. Drugs* 21 (2012) 1267–1308.
- [19] C. Singer, Managing the patient with newly diagnosed Parkinson's disease, *Clev. Clin. J. Med.* 79 (Suppl. 2) (2012) S3–S7.
- [20] J.W. Johnson, S.E. Kotermanski, Mechanism of action of memantine, *Curr. Opin. Pharmacol.* 6 (2006) 61–67.
- [21] J.H. Kurth, M.C. Kurth, Role of monoamine oxidase genetics in the etiology of Parkinson's disease, In: A. Lieberman, C.W. Olanow, M.B.H. Youdim, K. Tipton (Eds.), *Monoamine Oxidase Inhibitors in Neurological Diseases*, Marcel Dekker Inc., New York, 1994, pp. 113–126.
- [22] A. Whibley, J. Urquhart, J. Dore, L. Willatt, G. Parkin, L. Gaunt, G. Black, D. Donnai, F.L. Raymond, Deletion of MAOA and MAOB in a male patient causes severe developmental delay, intermittent hypotonia and stereotypical hand movements, *Eur. J. Hum. Gen.* 18 (2010) 1095–1099.

- [23] J.C. Shih, K. Chen, M.J. Ridd, *Ann. Rev. Neurosci.* 22 (1999) 197–217.
- [24] N. Castagnoli, J.P. Petzer, S. Steyn, K. Castagnoli, J.-F. Chen, M.A. Schwarzschild, C.J. Van Der Schyf, Monoamine oxidase B inhibitors and neuroprotection. *Neurology* 61 (Suppl 6) (2003) S62–S68.
- [25] A. Nicotra, F. Pierucci, H. Parvez, O. Senatori, Monoamine oxidase expression during development and aging, *NeuroToxicology* 25 (2004) 155–165.
- [26] L. Emilsson, P. Saetre, J. Balciuniene, A. Castensson, N. Cairns, E.E. Jazin, Increased monoamine oxidase messenger RNA expression levels in frontal cortex of Alzheimer's disease patients, *Neurosci. Lett.* 326 (2002) 56–60.
- [27] A.C. Tripathi, S. Upadhyay, S. Paliwal, S.K. Saraf, Privileged scaffolds as MAO inhibitors: Retrospect and prospects, *Eur. J. Med. Chem.* 145 (2018) 445–497.
- [28] M. Sadeghian, G. Mullali, J.M. Pocock, T. Piers, A. Roach, K.J. Smith, Neuroprotection by safinamide in the 6-hydroxydopamine model of Parkinson's disease. *Neuropathol. Appl. Neurobiol.* 42 (2015) 423–435.
- [29] M. Moravi, A. Brugnoli, C.A. Pisanò, S. Novello, C. Caccia, E. Melloni, G. Padoani, S. Vailati, M. Sardina, Safinamide differentially modulates in vivo glutamate and GABA release in the rat hippocampus and basal ganglia. *J. Pharmacol. Exp. Ther.* 364 (2018) 198–206.
- [30] E.D. Deeks, Safinamide: first global approval, *Drugs* 75 (2015) 705–711.
- [31] C. Cattaneo, R. La Ferla, E. Bonizzoni, M. Sardina, Long-term effects of safinamide on dyskinesia in mid-to late-stage Parkinson's disease: A post-hoc analysis, *J. Parkinson's Dis.* 5 (2015) 475–481.
- [32] H. Dvir, I. Silman, M. Harel, T.L. Rosenberry, J.L. Sussman, Acetylcholinesterase: from 3D structure to function, *Chem.-Biol. Interact.* 187 (2010) 10–22.
- [33] O. Lockridge, Review of human butyrylcholinesterase structure, function, genetic variants, history of use in the clinic, and potential therapeutic uses, *Pharmacol. Ther.* 148 (2015) 34–46.

- [34] N.H. Greig, D.K. Lahiri, K. Sambamurti, Butyrylcholinesterase: an important new target in Alzheimer's disease therapy, *Int. Psychogeriatr.* 14(Suppl. 1) (2002) 77–81.
- [35] D. Tewari, A.M. Stankiewicz, A. Mocan, A.N. Sah, N.T. Tzvetkov, L. Huminiecki, J.O. Horbanczuk, A.G. Atanasov, Ethnopharmacological approaches for dementia therapy and significance of natural products and herbal drugs, *Front. Aging Neurosci.* 10 (2018) A3.
- [36] E. Giacobini, Selective inhibitors of butyrylcholinesterase: a valid alternative for therapy of Alzheimer's disease? *Drugs Aging* 18 (2001) 891–898.
- [37] N.T. Tzvetkov, S. Hinz, P. Küppers, M. Gastreich, C.E. Müller, Indazole- and indole-5-carboxamides: selective and reversible monoamine oxidase B inhibitors with subnanomolar potency, *J. Med. Chem.* 57 (2014) 6679–6703.
- [38] N.T. Tzvetkov, Substituted indazole derivatives as in vitro MAO-B inhibitors, 2017, US Patent 9,643,930.
- [39] N.T. Tzvetkov, H.-G. Stammer, B. Neumann, S. Hristova, L. Antonov, M. Gastreich, Crystal structures, binding interactions, and ADME evaluation of brain penetrant N-substituted indazole-5-carboxamides as subnanomolar, selective monoamine oxidase B and dual MAO-A/B inhibitors, *Eur. J. Med. Chem.* 127 (2017) 470–492.
- [40] N.T. Tzvetkov, H.-G. Stammer, S. Hristova, A. G. Atanasov, L. Antonov, (Pyrrolo-pyridin-5-yl)benzamides: BBB permeable monoamine oxidase B inhibitors with neuroprotective effect on cortical neurons, *Eur. J. Med. Chem.* 162 (2019) 793–809.
- [41] D. Russo, N. Malafrente, D. Frescura, G. Imbrenda, I. Faraone, L. Milella, E. Fernandez, N. De Tommasi, Antioxidant activities and quali-quantitative analysis of different *Smilax* *sonchifolius* [(Poepp. and Endl.) H. Robinson] landrace extracts, *Nat. Prod. Res.* (2015) 29 1673–1677.

- [42] Q.C. Fidelis, I. Faraone, D. Russo, F.E.A. Catunda-Jr., L. Vignola, M.G. de Carvalho, N. De Tommasi, L. Milella, Chemical and biological insights of *Ouratea hexasperma* (A. St.-Hil.) Baill.: a source of bioactive compounds with multifunctional properties, *Nat. Prod. Res.* (2018) 1–4.
- [43] A. Holt, D.F. Sharman, G.B. Baker, M.M. Palcie, A continuous spectrophotometric assay for monoamine oxidase and related enzymes in tissue homogenates, *Anal. Biochem.* 244 (1997) 384–392.
- [44] J.G. Mohanty, J.S. Jaffe, E.S. Schulman, D.G. Raible, A highly sensitive fluorescent micro-assay of H<sub>2</sub>O<sub>2</sub> release from activated human leukocytes using a dihydroxyphenoxazine derivative, *J. Immunol. Methods* 202 (1997) 133–141.
- [45] Y.C. Cheng, W.H. Prusoff, Relationships between the inhibition constant ( $K_i$ ) and the concentration of inhibitor which causes 50% inhibition ( $IC_{50}$ ) of an enzymatic reaction, *Biochem. Pharmacol.* 22 (1973) 3099–3108.
- [46] E. Borroni, B. Bohmann, F. Grueninger, E. Prinssen, S. Nave, H. Loetscher, S.J. Chinta. S. Rajagopalan, A. Rane, A. Siddiqui, B. Ellenbroek, J. Messer, A. Pähler, J.K. Andersen, R. Wyler, A.M. Cesura, Sebragiline: A novel, selective monoamine oxidase type B inhibitor for the treatment of Alzheimer's disease. *J. Pharmacol. Exp. Ther.* 362 (2017) 413–423.
- [47] R.Z. Cer, U. Mudunuri, R. Stephens, F.J. Lebeda,  $IC_{50}$ -to- $K_i$ : a web-based tool for converting  $IC_{50}$  to  $K_i$  values for inhibitors of enzyme activity and ligand binding, *Nucleic Acids Res.* 37 (2009) W441–W445.
- [48] N.T. Tzvetkov, L. Antonov, Subnanomolar indazole-5-carboxamide inhibitors of monoamine oxidase B (MAO-B) continued: Indications of iron binding, experimental evidence for optimized solubility and brain penetration, *J. Enz. Inh. Med. Chem.* 32 (2017) 960–967.
- [49] W. Luo, Q.-S. Yu, S.S. Kulkarni, D.A. Parrish, H.W. Holloway, D. Tweedie, A. Shaffermann, D.K. Lahiri, A. Brossi, N. H. Greig, Inhibition of human acetyl- and butyrylcholinesterase by

- novel carbamates of (–)- and (+)-tetrahydrofurobenzofuran and methanobenzodioxepine, *J. Med. Chem.* 49 (2006) 2174–2185.
- [50] D. Lobner, Comparison of the LDN and MTT assays for quantifying cell death: validity for neuronal apoptosis? *J. Neurosci. Methods* 96 (2000) 147–152.
- [51] Z. Lin, Y. Will, Evaluation of drugs with specific organ toxicities in organ-specific cell lines, *Toxicol. Sci.* 126 (2012) 114–127.
- [52] N.T. Tzvetkov, H.-G. Stammler, L. Antonov, Tautomerism of N-(3,4-dichlorophenyl)-1H-indazole-5-carboxamide – A new, selective, highly potent and reversible MAO-B inhibitor, *J. Mol. Struct.* 1149 (2017) 273–281.
- [53] C. Binda, J. Wang, L. Pisani, C. Caccia, A. Carotti, P. Salvati, D.E. Edmondson, A. Mattevi, Structures of monoamine oxidase B complexes with selective non-covalent inhibitors: safinamide and coumarin analogs, *J. Med. Chem.* 50 (2007) 5848–5852.
- [54] M. Gastreich, C. Detering, L. Antonov, S. Hristova, H.-G. Stammler, N. T. Tzvetkov, New N-unsubstituted indazole-5-carboxamides as subnanomolar, selective monoamine oxidase B and dually active MAO-A/B inhibitors with BBB and GIT permeability, Abstracts of Papers of the American Chemical Society, Vol. 253, Amer. Chem. Soc., Washington, DC, 2017.
- [55] LeadIT v.2.3.2, BioSolveIT GmbH, Sankt Augustin, Germany, 2017. <http://www.biosolveit.de>.
- [56] SeeSAR v.9.0, BioSolveIT GmbH, Sankt Augustin, Germany, 2019. <http://www.biosolveit.de>.
- [57] G. Klebe, Applying thermodynamic profiling in lead finding and optimization, *Nat. Rev. Drug Discov.* 14 (2015) 95–110.
- [58] M. Betz, T. Wulsdorf, S.G. Krimmer, G. Klebe, Impact of surface water layers on protein–ligand binding: how well are experimental data reproduced by molecular dynamics simulations in a thermolysin test case, *J. Chem. Inf. Model* 56 (2016) 223–233.
- [59] Gaussian 09 (Revision D.01), M.J. Frisch, G.W. Trucks, H.B. Schlegel, G.E. Scuseria, M.A. Robb, J.R. Cheeseman, G. Scalmani, V. Barone, B. Mennucci, G.A. Petersson, H. Nakatsuji, M.

- Caricato, X. Li, H.P. Hratchian, A.F. Izmaylov, J. Bloino, G. Zheng, J.L. Sonnenberg, M. Hada, M. Ehara, K. Toyota, R. Fukuda, J. Hasegawa, M. Ishida, T. Nakajima, Y. Honda, O. Kitao, H. Nakai, T. Vreven, J.A. Montgomery, J.E. Peralta, Jr., F. Ogliaro, M. Bearpark, J.J. Heyd, E. Brothers, K.N. Kudin, V.N. Staroverov, R. Kobayashi, J. Normand, K. Raghavachari, A. Rendell, J.C. Burant, S.S. Iyengar, J. Tomasi, M. Cossi, N. Rega, J.M. Millam, M. Klene, J.E. Knox, J.B. Cross, V. Bakken, C. Adamo, J. Jaramillo, R. Gomperts, R.E. Stratmann, O. Yazyev, A.J. Austin, R. Cammi, C. Pomelli, J.W. Ochterski, R.L. Martin, K. Morokuma, V.G. Zakrzewski, G.A. Voth, P. Salvador, J.J. Dannenberg, S. Dapprich, A.D. Daniels, Ö. Farkas, J.B. Foresman, J. Ortiz, J. Cioslowski, and D.J. Fox, Gaussian, Inc., Wallingford CT, 2013.
- [60] Y. Zhao, D. Truhlar, Density functionals with broad applicability in chemistry, *Acc. Chem. Res.* 42 (2008) 157–167.
- [61] F. Weigend, R. Ahlrichs, Balanced basis sets of split valence, triple zeta valence and quadruple zeta valence quality for H to Rn: design and assessment of accuracy, *Phys. Chem. Chem. Phys.* 7 (2005) 3297–3305.
- [62] K. Kawauchi, L. Antonov, Description of the tautomerism in some azonaphthols, *J. Phys. Org. Chem.* 26 (2013) 643–652.
- [63] J. Tomasi, B. Mennucci, R. Cammi, Quantum Mechanical Continuum Solvation Models, *Chem. Rev.* 105 (2005) 2999–3094.
- [64] M. Savarese, É. Brémond, L. Antonov, I. Ciofini, C. Adamo, Computational insights into excited-state proton-transfer reactions in azo and azomethine, *ChemPhysChem* 16 (2015) 3966–3973.
- [65] Z. Rankovic, CNS physicochemical property space shaped by a diverse set of molecules with experimentally determined exposure in the mouse brain, *J. Med. Chem.* 60 (2017) 5943–5954.
- [66] D.E. Clark, Rapid calculation of polar molecular surface area and its application to the prediction of transport phenomena. I. Prediction of intestinal absorption, *J. Pharm. Sci.* 88 (1999) 807–814.

- [67] S. Vilar, M. Chakrabarti, S. Costanzi, Prediction of passive blood-brain partitioning: Straightforward and effective classification models based on in silico derived physicochemical descriptors, *J. Mol. Graphics Model.* 28 (2010) 899–903.
- [68] K.D. Freeman-Cook, Lipophilic efficiency: the most important efficiency metric in medicinal chemistry, *Future Sci.* 5 (2013) 113–115.
- [69] C. Abad-Zapatero, Ligand efficiency indices for effective drug discovery, *Expert Opin. Drug Discovery* 2 (2007) 469–488.
- [70] T.T. Wager, X. Hou, P.R. Verhoest, A. Villalobos, Central nervous system multiparameter optimization (CNS MPO) desirability: application in drug discovery, *ACS Chem. Neurosci.* 7 (2016) 767–775.
- [71] C.A. Lipinski, F. Lombardo, B.W. Dominy, P. J. Feeney, Experimental and computational approaches to estimate solubility and permeability in drug discovery and development setting, *Adv. Drug. Deliv. Rev.* 46 (2001) 3–26.
- [72] C. Aldrich, C. Bertozzi, G.I. Georg, L. Kiessling, C. Lindsley, D. Liotta, K.M. Merz, Jr., A. Schepartz, S. Wang, The ecstasy and agony of assay interference compounds. *J. Med. Chem.* 60 (2017) 2165–2168.
- [73] G.L. Ellman, K.D. Courtney, V. Andres-Jr., R.M. Featherstone, A new and rapid colorimetric determination of acetylcholinesterase activity, *Biochem. Pharmacol.* (1961) 7 88–95.
- [74] G.M. Sheldrick, A short history of SHELX, *Acta Crystallogr. A* 64 (2008) 112–122.
- [75] O.V. Dolomanov, L.J. Bourhis, R.J. Gildea, J.A.K. Howard, H. Puschmann, OLEX2: A complete structure solution, refinement and analysis program, *J. Appl. Crystallogr.* 42 (2009) 339–341.
- [76] M. Rarey, B. Kramer, T. Lengauer, G. Klebe, A fast flexible docking method using an incremental construction algorithm, *J. Mol. Biol.* 261 (1996) 470–489.

- [77] N. Schneider, G. Lange, S. Hindle, R. Klein, M. Rarey, A consistent description of HYdrogen bond and DEhydration energies in protein-ligand complexes: methods behind the HYDE scoring function, *J. Comput.-Aided Mol. Des.* 27 (2013) 15–29.
- [78] N. Schneider, S. Hindle, G. Lange, R. Klein, J. Albrecht, H. Briem, K. Beyer, H. Claußen, M. Gastreich, C. Lemmen, M. Rarey, Substantial improvements in large-scale redocking and screening using the novel HYDE scoring function, *J. Comput.-Aided Mol. Des.* 26 (2012) 701–723.
- [79] S. Bietz, S. Urbaczek, B. Schulz, M. Rarey, Protoss: A holistic approach to predict tautomers and protonation states in protein-ligand complexes, *J. Cheminform.* (2014) 6:12.
- [80] StarDrop, Optibrium Ltd., UK, 2019. [www.optibrium.com/stardrop](http://www.optibrium.com/stardrop).